iScience

CellPress
OPEN ACCESS

Article

Wafer-scale silver nanodendrites with homogeneous distribution of gold nanoparticles for biomolecules detection

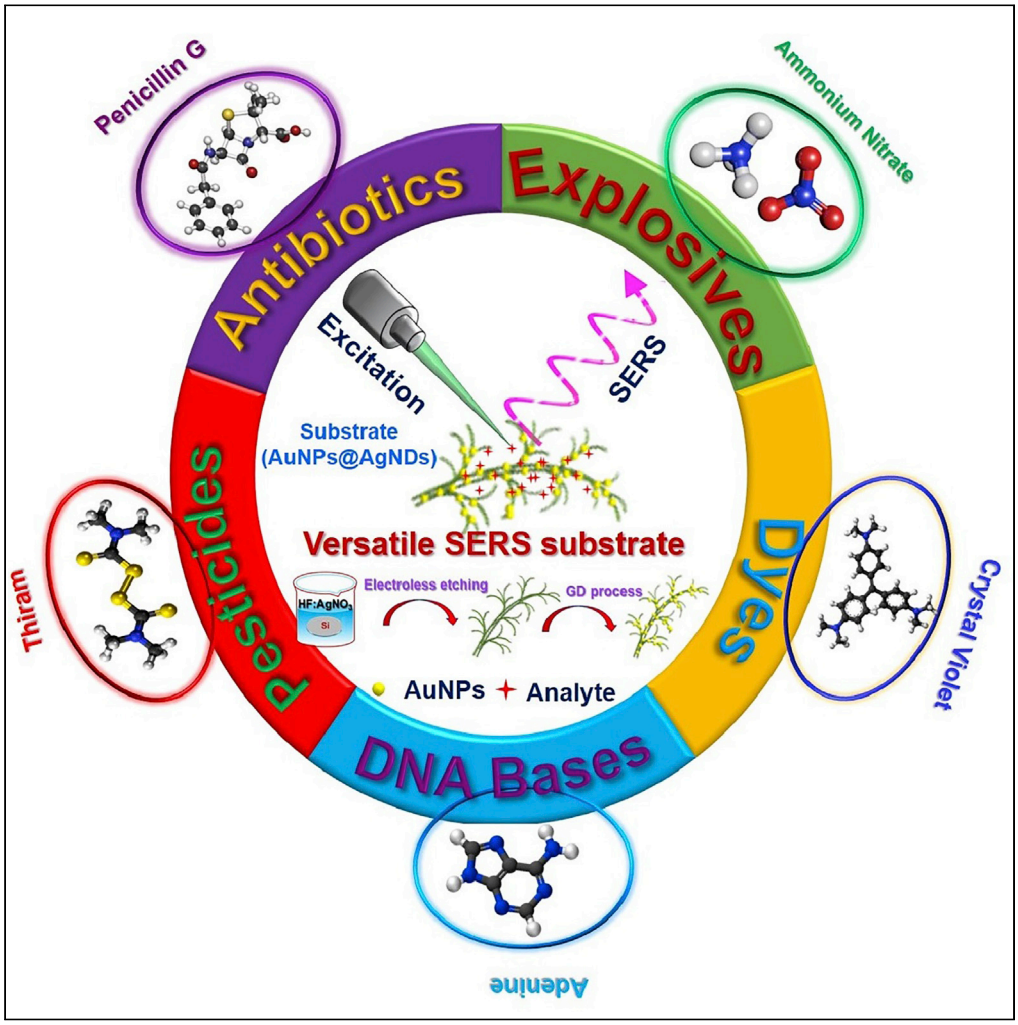

V.S. Vendamani, Reshma Beeram, M.M. Neethish, S.V.S. Nageswara Rao, S. Venugopal Rao

soma_venu@uohyd.ac.in, somavenu@gmail.com

Highlights

Wafer-scale surface-enhanced Raman spectroscopy/scattering (SERS) substrate of Ag nanodendrites decorated with Au nanoparticles prepared

Trace level detection of antibiotics achieved

Versatility of these substrates demonstrated by detecting explosive, dye molecules

Typical enhancement factors achieved were 10^5–10^7

Vendamani et al., iScience 25, 104849
August 19, 2022
https://doi.org/10.1016/j.isci.2022.104849

iScience

CellPress
OPEN ACCESS

Article

Wafer-scale silver nanodendrites with homogeneous distribution of gold nanoparticles for biomolecules detection

V.S. Vendamani,[1] Reshma Beeram,[1] M.M. Neethish,[2] S.V.S. Nageswara Rao,[3,4] and S. Venugopal Rao[1,5,*]

SUMMARY

We report the fabrication and demonstrate the superior performance of robust, cost-effective, and biocompatible hierarchical Au nanoparticles (AuNPs) decorated Ag nanodendrites (AgNDs) on a Silicon platform for the trace-level detection of antibiotics (penicillin, kanamycin, and ampicillin) and DNA bases (adenine, cytosine). The hot-spot density dependence studies were explored by varying the AuNPs deposition time. These substrates' potential and versatility were explored further through the detection of crystal violet, ammonium nitrate, and thiram. The calculated limits of detection for CV, adenine, cytosine, penicillin G, kanamycin, ampicillin, AN, and thiram were 348 pM, 2, 28, 2, 56, 4, 5, and 2 nM, respectively. The analytical enhancement factors were estimated to be $\sim 10^7$ for CV, $\sim 10^6$ for the biomolecules, $\sim 10^6$ for the explosive molecule, and $\sim 10^6$ for thiram. Furthermore, the stability of these substrates at different time intervals is being reported here with surface-enhanced Raman spectroscopy/scattering (SERS) data obtained over 120 days.

INTRODUCTION

Raman spectroscopy is a conventional and adaptable analytic technique to diagnose characteristic signatures, the structure of analytes, as well as interfacial reactions in areas of interest such as medical diagnosis, chemical analysis, environmental monitoring, food safety, and defense, and so forth. (Wu et al., 2013; Yang et al., 2016; Bremer and Dantus, 2013; Portnov et al., 2008; Dubey et al., 2021). However, the detection of biological species is often complicated and liable to interference with another molecule of interest. Ideally, a label-free investigation is necessary for the direction of biomarker detection. Surface-enhanced Raman spectroscopy/scattering (SERS) is one of the most fascinating analytic techniques for rapid, in-field, single-shot detection of analyte molecules finding impending applications in biomedicine, clinical, environmental detection, food safety, and so forth. (Vendamani et al., 2022; Verma and Soni, 2022; Tzeng and Lin, 2020; Zhang et al., 2013; Powell et al., 2017; Ouyang et al., 2018; Xu et al., 2018; Zhu et al., 2021). This technique has also been favored in food inspection via examining antibiotic deposits in animal products (Lirio et al., 2016; Li et al., 2015). SERS is one of the most versatile, label-free analytical techniques for rapid, in-field detection of biomolecules in a single shot experiment. Bio-compatible noble metal (Ag/Au) based SERS-active substrates are highly desirable and potential intrants for the investigation of a variety of biomolecules. Food safety is probably one of the most profound aspects of human life in the category of safety concerns. In this circle of a topic, it is appalling that many millions of people worldwide have been affected by contaminated food substances. Hence, with the rapid developments in the modern world, chemical, environmental, and microbiological contaminants are significant pollutants that should be moderated and detected easily. The rapid growth and involvement of molecular sensing encouraged numerous researchers to explore various technologies toward the fabrication of economical, reproducible, and highly sensitive SERS-active substrates for label-free molecular detection (Vendamani et al., 2018a, 2018b, Ravi Kumar et al., 2021; Moram et al., 2018; Bharati et al., 2018; Beeram et al., 2022; Rathod et al., 2022; Banerjee et al., 2022). The plasmonic nanostructures (NSs) with different dimensions on rough surfaces attracted researcher's interests owing to the exploration of SERS by Fleischmann et al. in the seventies, witnessed through Raman enhancement of pyridine in the order of $\sim 10^6$ on a rough metal silver electrode (Fleischmann et al., 1974). There are various plasmonic NSs, such as single metallic nano-spheres, nano-wires, nano-pyramids, nano-stars, bimetallic nano-mushrooms, alloy nano-particles, and so on, which have been recommended as a SERS substrate for attempting incredible efforts on molecular sensing via

[1]Advanced Centre for Research in High Energy Materials (ACRHEM), University of Hyderabad, Hyderabad 500046, India

[2]Department of Physics, Pondicherry University, Puducherry 605014, Puducherry, India

[3]Centre for Advanced Studies in Electronics Science and Technology (CASEST), University of Hyderabad, Hyderabad 500046, Telangana, India

[4]School of Physics, University of Hyderabad, Hyderabad 500046, Telangana, India

[5]Lead contact

*Correspondence: soma_venu@uohyd.ac.in, somavenu@gmail.com

https://doi.org/10.1016/j.isci.2022.104849

localization of the electromagnetic field (Velazquez-Salazar et al., 2019; Tim et al., 2021; Bora, 2018; Sun et al., 2019; Tao and Yang, 2005; Barbillon, 2020; Shen et al., 2014; Yu et al., 2020; Zhang et al., 2016). The fundamental properties and behavior of plasmonic NSs can be modulated by altering their sizes, shapes, and dimensions (Amiens et al., 2016; Burda et al., 2005; Kelly et al., 2003). Indeed, this can enrich the application prospects in diverse fields such as optoelectronics, catalysis, energy, environment, and detection (Velazquez-Salazar et al., 2019; Tim et al., 2021; Bora, 2018; Sun et al., 2019; Tao and Yang, 2005; Barbillon, 2020; Shen et al., 2014; Yu et al., 2020; Zhang et al., 2016).

Recently, enormous efforts have been disseminated in formulating different architectures of silver-based NSs (e.g., AgNPs, Ag nanoflowers, core-shell NSs, dendrites, and other complex nanostructures) for the SERS activity because of its strong inter-particle near field coupling effects and strong surface plasmon resonances in the visible to the near-infrared spectral regime (Ma et al., 2020; Li et al., 2012; Chaudhari et al., 2018; Wei et al., 2018; Tian et al., 2019; Jiang et al., 2017; Verma and Soni, 2021; Podagatlapalli et al., 2015; Ceballos et al., 2022). Among the existing AgNSs, silver nano-dendrites (AgNDs) have occupied a particular spot in SERS-based sensing applications spotted owing to their outstanding properties such as (a) ease of synthesis (b) adaptability (c) specific surface area (d) cost-effectiveness, (e) broadband hot electron generation, and so forth. (see, for example, Bandarenka et al., 2020; Yakimchuk et al., 2019; Zhao et al., 2016; Lo Faro et al., 2019; Cheng et al., 2019a, 2019b, 2019c; Wang.et al., 2021). The AgNDs, possessing fractal structures with multi-level branches and trunks can produce tunable multi-band resonances for localized near-field enhancements along with a provision for the presence of randomly distributed multiple hot-spots (Huang et al., 2015a, 2015b; Wang et al., 2021; Cheng et al., 2019a, 2019b, 2019c). These multi-level branching structures typically offer inter-branch gaps/junctions, corners, edges, and high surface-to-volume ratio making them suitable for surface-sensitive applications such as surface plasmon resonance-based sensing, SERS, and catalysis (Cheng et al., 2019a, 2019b, 2019c; Kima et al., 2017; Gu et al., 2015; Cheng et al., 2020). Therefore, in comparison with smooth SERS-active surfaces, multi-level branched NDs have reached maturity and provide an excellent opportunity for SERS-based sensing in the chemical industry, food safety, environmental pollutants, and biomedical applications (Bandarenka et al., 2020; Yakimchuk et al., 2019; Zhao et al., 2016; Lo Faro et al., 2019; Cheng et al., 2019a, 2019b, 2019c).

Electroless etching is a recognized wet etching process to prepare AgNDs on a solid platform. In recent years silicon has frequently been used as a reducing agent owing to its versatility, superior bio-compatibility, and multi-functionality (Weakliem and Redfield, 1979; Ngan et al., 2017; Kuntyi et al., 2019). According to the Scopus research report retrieved recently, there were >60 articles on AgNDs that originated from SERS sensing in the last five years. However, Ag NSs suffer from lower chemical stability and are highly sensitive toward oxidation (during exposure to ambient atmosphere), which can deteriorate the operating lifetime of Ag-based SERS substrates (Huang et al., 2015a, 2015b; Khaywah et al., 2015). To circumvent these limitations and improve the long-term accessibility of AgNDs in sensing, it is imperative to passivate/decorate them (Yin et al., 2015; Gutes et al., 2012). For this approach, we have considered gold nanostructures (AuNSs) that have exhibited excellence in surface passivation owing to their feasible dimensionality, biocompatibility, high stability, various functionality, and reusability in specific cases and outstanding tunability of the optical properties in the visible and near-infrared frequencies. In this process, several research articles focused recently on the design of bimetallic Ag/Au hybrid NSs such as Au@Ag nanorods, Ag-Au-PVA thin films, and Au-Ag core-shell for the betterment of SERS-activity with good stability and ultra-sensitivity (Rao and Radhakrishnan, 2015; Pastorello et al., 2020; Samal et al., 2013). Therefore, the uniform distribution of AuNSs over the targeted surface is highly essential for effective productivity.

AuNPs and AuNSs are accentuated among the existing NSs for various applications and there are various methods such as atomic layer deposition, laser ablation, sputtering, and so forth, that exist in the literature for preparing them (Byram et al., 2019; Hatakeyama et al., 2011; Hashemi et al., 2020; Palazzo et al., 2017). By counting on the cost-effectiveness and ease of handling, the preparation of AuNPs favors a facile galvanic displacement (GD) process, which results in the homogeneous distribution of NPs over the aimed surface (Gutes et al., 2011; Srikanth and Jeevanandam, 2012; Shepida et al., 2019; Magagnin et al., 2002; Zhang et al., 2015). The existing findings in the literature on Au and AgNSs motivated us to fabricate bimetallic Au/Ag nanostructures by combining a facile electroless and galvanic deposition process. It has been demonstrated recently that the synergistic effects of both AuNPs chemical stability and the AgNDs strong plasmonic effects have considerably improved the SERS activity and time stability (see, for example, Huang et al., 2015a, 2015b; Khaywah et al., 2015; Yin et al., 2015). We have performed comprehensive

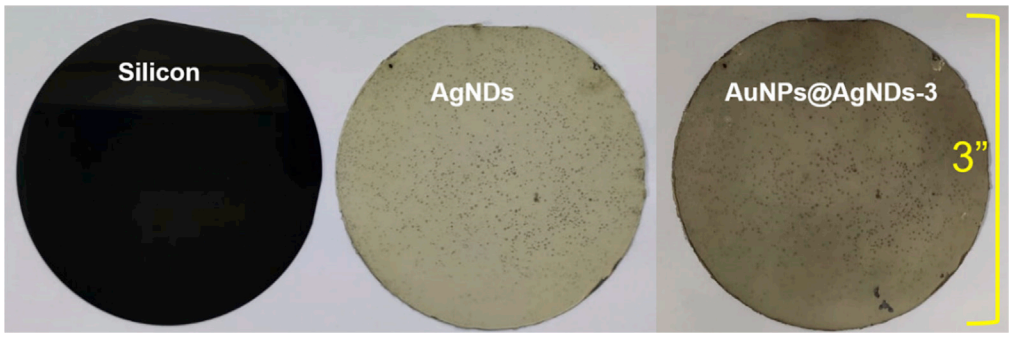

Figure 1. Photographs of the bare three inches Si wafer (left), AgNDs on Si wafer (middle), and AuNPs@AgNDs on Si wafer (right). The AuNPs were decorated in ~3 h (i.e., AuNPs@AgNDs-3)

investigations on the formation of AuNPs@AgNDs while varying the AuNPs density (deposition time) and their application toward trace level detection of diverse biomolecules such as antibiotics (penicillin, kanamycin, and ampicillin), DNA bases (adenine, cytosine), an explosive molecule (ammonium nitrate - AN), and thiram, a pesticide molecule along with time-stability studies. Our experimental results demonstrate that the bimetallic AuNPs@AgNDs nanostructures can be highly efficient for excellent SERS activity. To the best of our knowledge, no reports are available on the detection of antibiotics using AuNPs decorated AgNDs. Furthermore, we have demonstrated the preparation of these substrates on a large scale (3 inches wafer) with no limitations. This could be easily extended to six-inch wafers and that could be prepared in 30 min.

Experimental procedures

Materials and chemicals

A three inch p-type, boron-doped single-crystal Si wafers with a resistivity of 1–10 Ω-cm were purchased locally (M/s Macwin India) and appropriately cleaned before use. The silver salt ($AgNO_3$) from Finar, ethanol (reagent grade), and highly concentrated hydrofluoric acid (48%HF) were purchased from Merck. The $AuCl_4{:}3H_2O$, antibiotics (Penicillin G-$C_{16}H_{18}N_2O_4S$, Kanamycin- $C_{18}H_{36}N_4O_{11}$, Ampicillin-$C_{16}H_{18}N_3NaO_4S$), and DNA bases (Adenine- $C_5H_5N_5$, Cytosine- $C_4H_5N_3O$) with a purity of 99.99% were purchased from M/s Sigma-Aldrich. The dye molecule crystal violet ($C_{25}N_3H_{30}Cl$) and Thiram ($C_6H_{12}N_2S_4$) were also obtained from Sigma-Aldrich. The explosive molecule, Ammonium Nitrate (NH_4NO_3), used for SERS studies was procured from the High Energy Materials Research Laboratory (HEMRL), Pune, India.

Synthesis and characterization of surface-enhanced Raman spectroscopy/scattering substrates

Silver nano-dendrites are synthesized by adopting low-cost, simple methodological electroless-etching; the details of which are described in one of our earlier reports (Vendamani et al., 2020). In brief, a three″ Si wafer has been cleaned with acetone and diluted HF to remove chemical residues and native oxide, respectively. The cleaned Si wafer is immersed in (30 mM) $AgNO_3$ and (4.6 M) HF composed electrolytic solution for dendrite formation at 30°C. Followed by dendrite samples are cleaned with DI water and dried in an ambient atmosphere. The cleaned three″ AgNDs sample was fragmented to a 1 cm^2 model for subsequent studies. The stability, compatibility, sensitivity, and commercialization of these AgNDs substrates are believed to be greatly enriched by incorporating gold AuNPs under the facile galvanic deposition approach. This wet-chemical process permits precise control of the size, shape, and distribution of NPs, allowing for enhanced plasmonic behavior for superior bio-sensing. In the direction of viable SERS-active substrate design, the critical factor of hot-spots regions was improved by increasing the density of AuNPs on 1 cm^2 AgNDs at 30 min, 1 h, 2 h, 3 h immersion time in 1 mM $HAuCl_4$:5 mM HF solution, and the corresponding sample tags are AuNPs@AgNDs-0.5, AuNPs@AgNDs-1, AuNPs@AgNDs-2, AuNPs@AgNDs-3, respectively.

The dense bimetallic hot-spots generated at 3 h (AuNPs@AgNDs-3) were identified to be highly desirable for obtaining an effective Raman signal from the biomolecules. The resulted 1 cm^2 sample was equally divided into four pieces for subsequent characteristic investigations. The optical images of the three″ plain Si wafer, AgNDs sample, and the AuNPs@AgNDs-3 are shown in Figure 1. The AgNDs obtained with 3 h AuNPs immersion time (i.e., AuNPs@AgNDs-3) were utilized for further characteristic investigations. It started with a morphological examination using a field emission scanning electron microscope (FESEM; Carl ZEISS, Ultra 55–5 eV for imaging, and 20 eV for EDX). The corresponding elemental mapping was performed on AgNDs using the

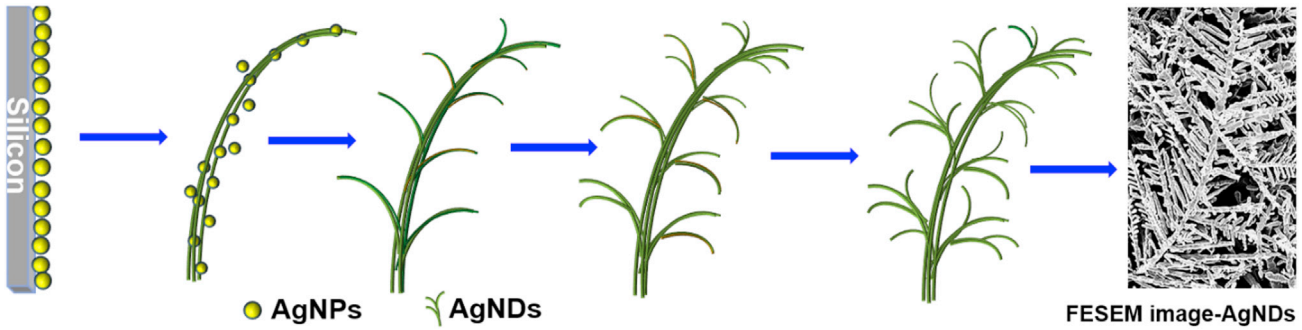

Figure 2. Graphical representation showing the growth of single AgNDs formation over the time of electroless etching (In the present report, the etching time is 15 min)

Energy-dispersive X-ray spectroscopy (EDS) technique. X-ray photoelectron spectroscopy (XPS) analysis was accomplished using a Thermo Scientific (K-Alpha-KAN9954133) instrumental setup to confirm the metallic Ag nature of the formed structure. Transmission electron microscope (TEM; Technai, equipped with a thermo-ionic electron gun working at 200 keV) and X-ray diffraction (XRD-Bruker D8 advance) investigations were used to confirm the crystalline quality of the AgNDs and AgNDs@AuNPs. The optical reflection was evaluated by a UV-Visible spectrophotometer (UV–Vis–Jasco V-670) to identify the surface plasmon resonance band for different SERS activities. A micro-Raman spectrophotometer (Horiba LabRam Raman Spectrometer) was employed to study essential aspects of molecular detection under Nd: YAG laser excitation. The SERS activity has been tested with various kinds of probe molecules like (i) dyes (crystal violet - CV) (ii) explosives (ammonium nitrate - AN) (iii) pesticides (thiram) and (iv) biomolecules, especially DNA bases (adenine, cytosine), which could be a DNA and RNA builder and tracing of these solutions is essential in biomarker investigations, and antibiotics (penicillin-G, kanamycin, and ampicillin) are effective in preventing and treating infections in humans and animals (Chen et al., 2017; Jiang et al., 2019). In 1999, European Union established the maximum residue limits (MRL) of antibiotics in foodstuff which was 4 μg/kg of penicillin-G and 150 μg/kg kanamycin. In the present study, we could achieve a limit of detection that is compatible with the requisite MRL values. For achieving a better consistency in the Raman signal, the measurements were performed using a 50× objective, 10 s acquisition time, and using 532 nm excitation. The spot size estimated at the focus was ~1.5 μm. Eventually, the visualization of the near-field enhancement around the NDs was explored by simulations with the support of COMSOL.

Substrate preparation for measurements

As prepared AgNDs were ultrasonicated in ethanol and drop-casted on Cu grids for the TEM measurements. The antibiotics and adenine molecules were dissolved in Milli-Q water to make a stock solution. Furthermore, required concentrations of analytes were diluted from the stock solution. The solution of analytes (~20 μL) was drop-casted on SERS-active (AuNPs@AgNDs-3) substrate for subsequent SERS investigations. For real-time stability studies, a 20 μL CV analyte was drop-casted on the same substrate at various intervals and up to 120 days of ambient exposure.

RESULTS AND DISCUSSION

A straightforward electroless deposition process formed many silver nano-dendrites (AgNDs) on the Si wafer. Electroless etching and immersion baths are easy to handle and used in achieving a high density of hot-spot locations, which are highly desirable for trace-level molecular sensing. AgNDs prepared at various $AgNO_3$ molar concentrations and different etching temperatures were demonstrated in our earlier report (see Vendamani et al., 2020). The dendrite nanostructure comprises primary and secondary branches attached to the central stem. The generated AgNDs were highly symmetric with 8 and 6 μm primary and secondary branches, respectively. The angle between the stem and branches was in the range of 50°–65°. The schematic representation shown in Figure 2 illustrates the growth of AgNDs formation over different times of the electroless etching process.

This structure was further decorated with AuNPs to generate strong field points effectively. Also, AuNPs deposition results in surface passivation owing to its dimensionality, bio-compatibility, high stability, lower oxidation effect, various functionality, reusability in specific cases, and outstanding tunability of the optical properties in the visible and near-infrared frequencies. Figure 3A illustrates the growth of AgNDs at 30 mM

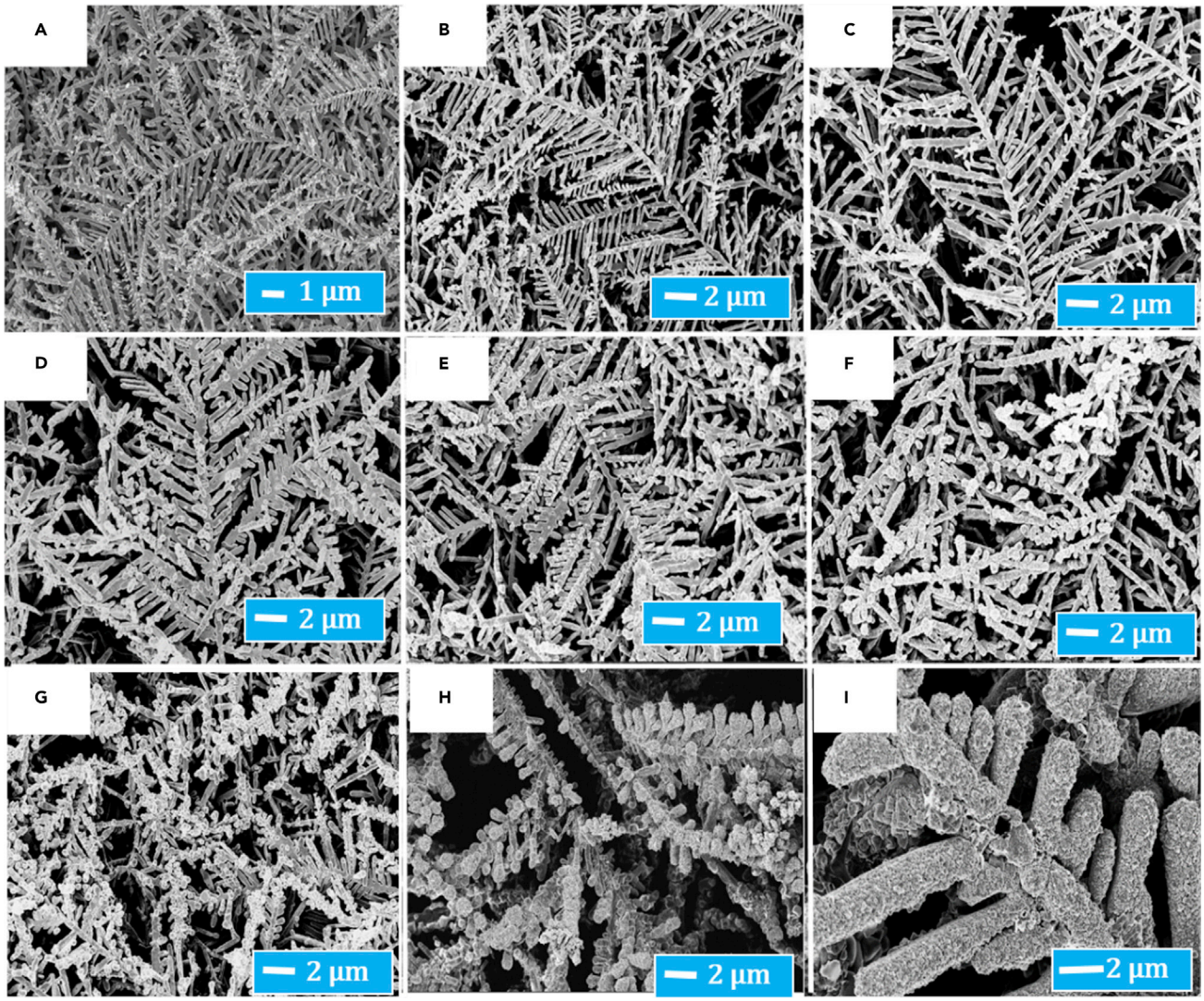

Figure 3. FESEM images of AgNDs with AuNPs at different concentrations of Au seed solutions

FESEM images of (A) as prepared AgNDs and AuNPs decorated AgNDs at various molar concentrations of Au seed solutions at (B) 0.05 mM, (C) 0.1 mM, (D) 0.5 mM, (E) 1 mM, (F) 1.5 mM, (G) 3 mM, (H) 5 mM, (I) 7 mM at room temperature.

$AgNO_3$ concentration and Figures 3B–3I represents the fixed deposition time (i.e., 15 min) of AuNPs at various molar concentrations (i.e., 0.05, 0.1, 0.5, 1, 1.5, 3, 5, 7 mM, respectively) of gold seed solution. The data presented demonstrate that on increasing the gold solution, the decoration of the AuNPs on the walls of AgNDs was noticeably increased.

At lower concentrations of the gold solution (data shown in Figures 3B–3E), a sparse layer of Au NPs was observed on AgNDs. With increasing concentration levels, especially at 1.5 mM, apparent changes in the density of AuNPs decoration were observed, as shown in Figure 3F. The higher density of AuNPs grew at 3 mM to cover almost the whole dendrite structure, as shown in Figure 3G. When we proceeded to higher concentrations such as 5 mM, 7 mM (data shown in Figures 3H and 3I), the AuNPs have completely concealed the dendrite structure, which may not be apposite for the SERS measurements owing to the absence of dendritic nature. After keen examination of all the concentrations of AuNPs, we deliberately chose the optimistic AuNPs deposition at 1 mM concentration with isolated and uniform distribution.

For a detailed understanding, we aimed to investigate the effect of AuNPs (1 mM concentration) deposition time for density dependence correlation. Figure 4 represents the FESEM micrographs of AgNDs at

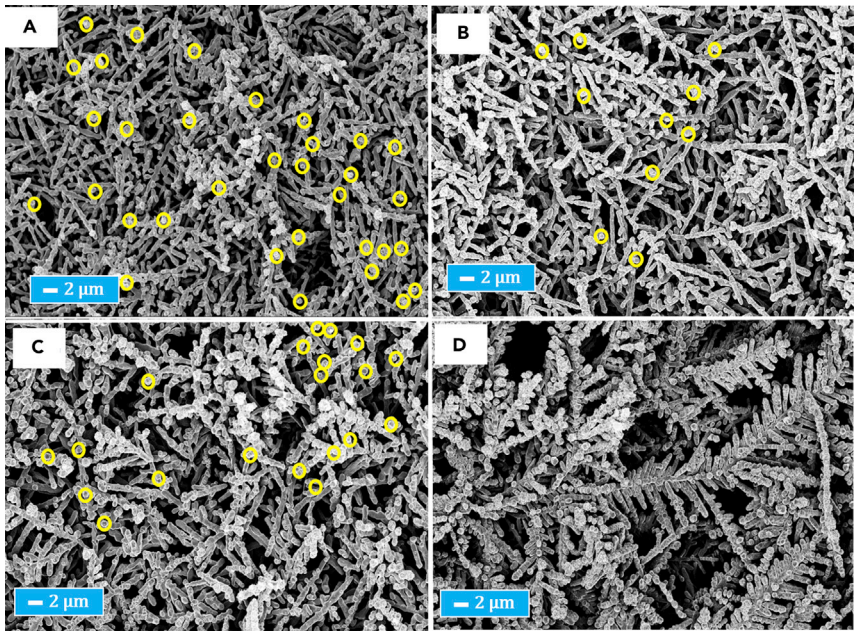

Figure 4. FESEM images of AgNDs with AuNPs at different times of deposition

SEM images displaying morphology of the AgNDs decorated with 1 mM AuNPs at various times of deposition (A) 30 minutes (i.e., AuNPs@AgNDs-0.5), (B) 1 h (i.e., AuNPs@AgNDs-1), (C) 2 h (i.e., AuNPs@AgNDs-2), and (D) 3 h (i.e., AuNPs@AgNDs-3) (highlighted yellow-coloured circles represent the AuNPs decoration on AgNDs at a few places for clarity).

different AuNPs deposition times, varying from 30 min to 3 h. Figure 4A displays the few isolated AuNPs (deposition at 30 min) over the sample surface. At the consequent deposition at 1 h and 2 h, well-isolated AuNPs partially covered the branches of AgNDs as shown in Figures 4B and 4C. Interestingly, as the reaction time proceeded to 3 h, the distribution of AuNPs was homogeneous and the amount of AuNPs increased progressively (image shown in Figure 4D). This indicated that the high density of AuNPs on AgNDs at 3 h could elevate the strength of the Raman signal by exhibiting strong surface plasmonic resonance compared to other reaction times. We believed that these 3D plasmonic nanostructures not only generate efficient field hot-spots but could also contribute to adsorption of target analytes owing to the large surface availability. These features are substantial for attaining superior SERS activity. The highly qualified samples were subsequently used for further characteristic examinations.

Figure 5A–5C present the different magnification images of AuNPs decorated at 3 h of reaction time (AuNPs@AgNDs-3), which clearly illustrate the morphological features in detail. Furthermore, the elemental identification of AuNPs@AgNDs-3 was carried out by performing the EDX mapping; the data of which is shown in Figure 6. It is extracted from the EDX mapping data that the dominant peak corresponds to Ag, with multiple Au signals from AuNPs, and Si (as expected from the base substrate). In addition, oxygen and minute carbon impurities were observed owing to natural oxidation and the solvents used. Following the compositional examination, the metallic nature of prepared AgNDs and AuNPs coated AgNDs is examined by recording XPS survey scans. Figure 7A shows the typical comprehensive scan, depicting the peaks at 99, 150, 573, 68, 84 eV, which are attributed to the Si 2p, Si 2s, Ag 3p, Ag 3days, and Au 4f, respectively. Although oxygen and carbon signals have also been noticed, they were present in the samples only at lower concentrations. The data presented in Figure 7B illustrates the significant Ag signals, such as the Ag 3d doublet line with binding energies of 368.2 eV for Ag $3d_{5/2}$ and 374.2 eV for Ag $3d_{3/2}$, Ag auger peaks (573.5 eV for Ag 3p1, 604.3 eV for Ag 3p3), and low-intensity plasmon loss peaks (represented as *) indicating the metallic nature of AgNDs being formed under electroless etching. Figure 7C demonstrates the XPS data confirming the successful formation of AuNPs deposition at various deposition times over the AgNDs surface. Au 4f XPS spectra exhibited two asymmetric peaks, Au $4f_{7/2}$ at 84.1 eV and Au $4f_{5/2}$ at 87.8 eV, with a splitting of 3.7 eV confirming the Au metallic bond (Li et al., 2018). The other signal at 83.22 eV is attributed to metallic alloy formation at the Au-Ag interface and is not observed in Figure 7C.

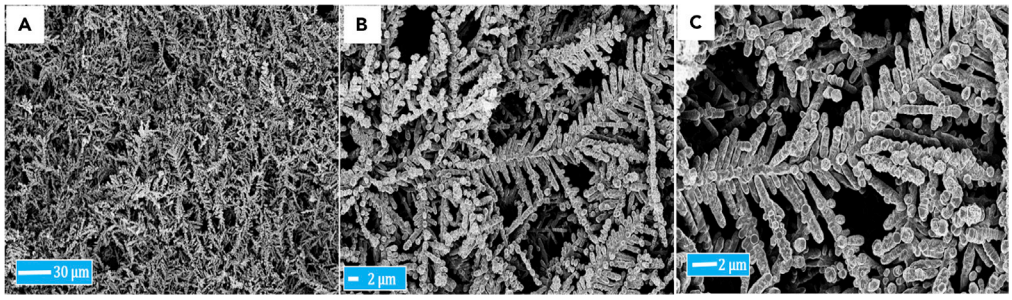

Figure 5. SEM images of the AuNPs (on AgNDs) decorated at 3 h reaction time (AuNPs deposited at 1 mM concentration) (i.e., AuNPs@AgNDs-3) viewed at different magnifications

Furthermore, the atomic percentage of gold has been quantified under XPS analysis. It is addressed to be increased progressively as on improving the Au deposition time as expected, the data of which is presented in Figure 7D.

XRD and TEM data were used to investigate the crystallinity of the prepared AgNDs. Figure 8 shows typical XRD diffraction patterns of AgNDs and AuNPs@AgNDs substrates. AgNDs deliver well-crystallized face-centered cubic structures, which are characterized by a set of reflections from planes of (111), (002), (220), (022), (004), (113), and (222) (JCPDS Card No.98-005-0882). The response at (002) with a slight broadness represents the polycrystalline nature of AgNDs. The observed high-intensity peak (111) in the spectra implies that the growth direction was predominantly along the crystal plane. All the spectra are stacked and normalized (with respect to the intensity) for a clear spectral representation. The normalized intensity of the significant peak at (111) is attributed to the presence of Ag and Au, which were found to be increasing with growing AuNPs deposition time. Likewise, the deposition of AuNPs over AgNDs was confirmed and indexed the peak at (222). Figure 9A (TEM image) shows clear morphological evolutions of AgNDs, which consisted of trunks and branches with definite directions (about 60° angles concerning the central trunk). These features are consistent with those observed in the FESEM images. The IFFT image shown in Figure 9D was collected from the yellow dotted rectangular line indicated on the HRTEM image (shown in Figure 9C). The estimated inter-planar spacing between lattice fringes of AgNDs was ~0.24 nm, which corresponds to the Ag's (111) crystal plane. Furthermore, it endorses the predominant growth direction of AgNDs along the (111) plane. The SAED pattern depicted in Figure 9B exhibits the single-crystal nature of AgNDs, which is in good agreement with the XRD investigations.

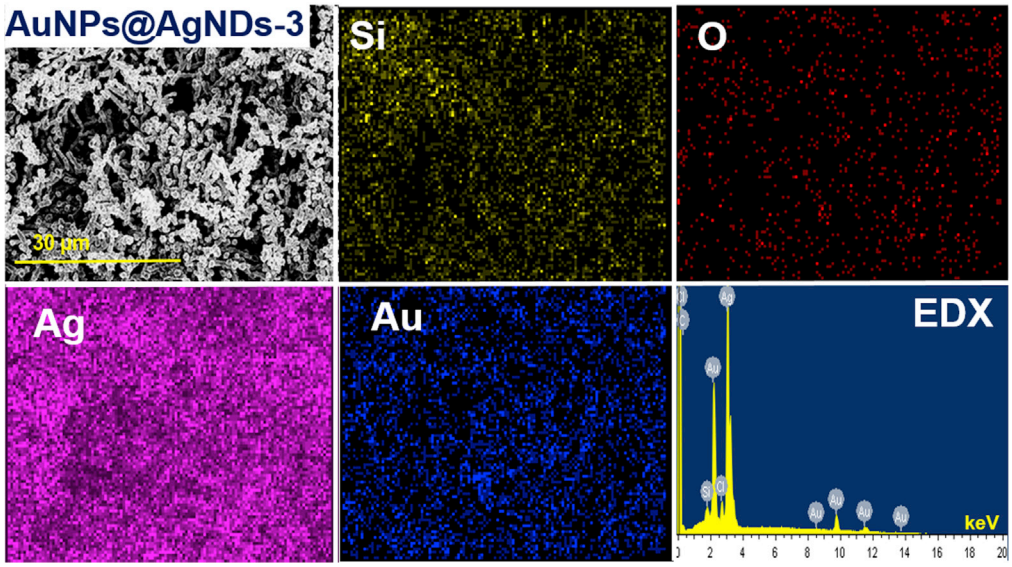

Figure 6. EDX mapping presents the elemental composition of the AuNPs@AgNDs-3 sample, which depicts a high concentration of Ag, Au, and Si, and a lower concentration of O as expected

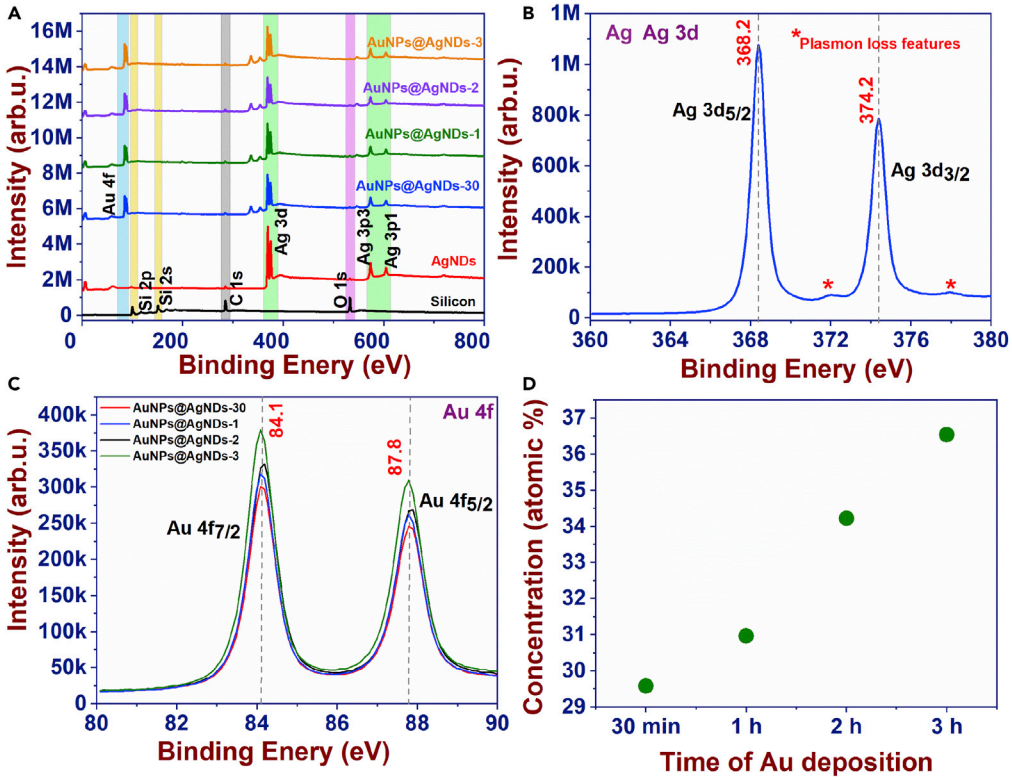

Figure 7. XPS data of Si, AuNDs and AuNDs + AuNPs

XPS survey scan data of (A) bare silicon, AgNDs, and AuNPs coated AgNDs, (B) XPS presents specially plotted Ag nanodendrites (small portion of the data taken from (A)), (C) XPS data of AuNPs @AgNDs at different times of AuNPs deposition, and (D) the atomic percentage of elemental gold over the time of deposition.

The reflection properties of AgNDs and AuNPs capped AgNDs are shown in Figure 10. It is noticed that the reflection decreased with increasing time of the AuNPs deposition on AgNDs, which is owing to a change in the surface roughness. After keen observations of reflection data, we concluded that the AuNPs@AgNDs-3 sample has demonstrated lower reflection properties at lower wavelengths. Besides, for anisotropic structures such as AgNDs there is a longitudinal and transverse SPR band. The longitudinal band occurs at higher wavelengths relative to the transverse band in elongated structures. In our case 426 nm corresponds to transverse mode and 696 nm corresponds to longitudinal mode of AgNDs (Agustina et al., 2020; Bijanzadeh et al., 2012; Cheng et al., 2019a, 2019b, 2019c; Wang et al., 2021). The dip is predominant for longitudinal mode relative to the transverse mode indicating a greater anisotropy. The dip at 464 nm is weak and needs further investigations to exactly assign it. This peak could be owing to the different sizes, shapes, and configurations of the AuNPs on AgNDs which themselves are available in different sizes and shapes. For Ag-based fractal structures like dendrites, multiple resonance peaks were reported previously (Wang et al., 2021; Cheng et al., 2019a, 2019b, 2019c). Similarly, the characteristics of AgNDs were dominated by branches with high aspect ratios, which are responsible for the longitudinal bands observed in the higher wavelength regions. The positions of SPR bands contribute to maximum electric field strength, which helps identify a suitable excitation wavelength with better resonant conditions for SERS measurements on these AgNDs-based active substrates. The excitation wavelength at 532 nm has been considered after evaluating the UV-Visible data for further investigation of the SERS study.

SERS performance is a critical parameter to understand and evaluate the quality of substrates. Hence, we have evaluated the SERS activity of AuNPs@AgNDs-3 substrates by subjecting diverse molecules like dye, explosives, DNA bases, and antibiotics as probing molecules. In the first stage, to evaluate the substrate quality in terms of sensitivity and capability, the active substrates were subjected to basic cationic dye molecule as CV, because it has strong absorption in the visible region under 532 nm laser excitation. Figure 11A depicts the concentration-dependent (10 μM–1 nM) plot on the active substrate, in which the

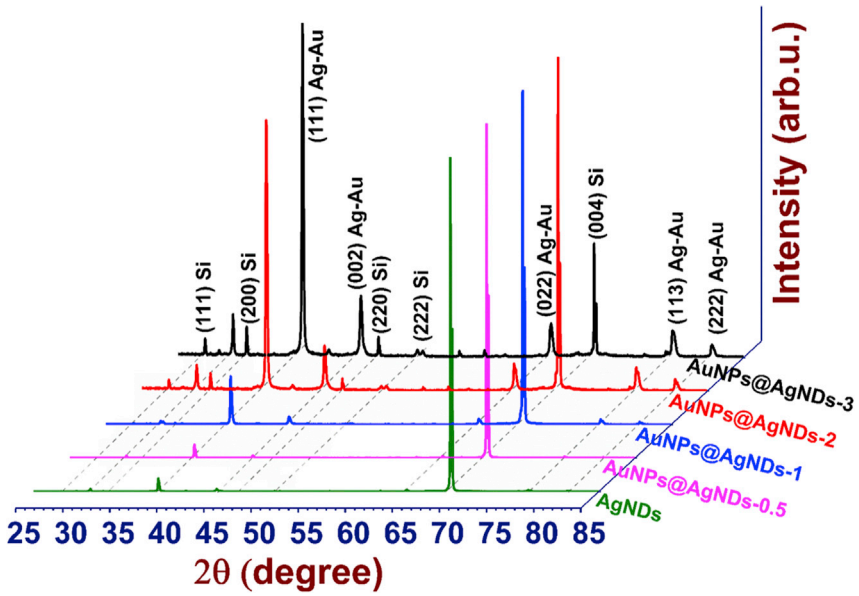

Figure 8. X-ray diffraction (XRD) pattern of AgNDs and AuNPs decorated AgNDs at various deposition times

vibrational modes of CV were identified at 918 cm^{-1}, 1181 cm^{-1}, and are assigned following the literature (Fateixa et al., 2018). The details of the modes observed and assignments are summarized in Table S2. A significant intensity change was noticed in the primary characteristic peak at 918 cm^{-1}, which demonstrates that the intensity gradually decreased with a decrease in the concentration, which was expected. The log intensity versus analyte at lower concentrations of the Raman mode at 918 cm^{-1} was estimated to be linear with an R^2 of 0.99; the data being presented in Figure 11B. Apart from the SERS activity of substrate, the most prominent factor is to assess the degree of sensitivity by evaluating the analytical enhancement factor (AEF) by the inclusion of adsorption factor η (which is extracted from the intensity versus concentration plot) in the standard formula described in our earlier reports (Hamad et al., 2014; Shaik et al., 2016; Vendamani et al., 2021). The evaluated AEF for 1 nM CV was ~3.2×10^7, which is shown in Table 1.

Furthermore, the SERS based on plasmonic nanostructures could pave an effective way to analyze DNA bases such as adenine and cytosine. Adenine is an energy source for human cells, which could be a DNA and RNA builder. In this regard, the trace detection of adenine solution is essential in biomarker investigations. Figure 12A illustrates the SERS spectra of adenine with concentration range from 1 mM to 100 nM range; it is discerned that the intensity value drops down while approaching trace level concentration. The Raman modes were observed at 534 cm^{-1}, 621 cm^{-1}, 722 cm^{-1}, 1125 cm^{-1}, 1246 cm^{-1}, 1330 cm^{-1}, 1481 cm^{-1}, and the corresponding vibrations are shown in Table S2 (Madzharova et al., 2016). The intensity of the significant characteristic peak of adenine at 722 cm^{-1} was observed even at a lower concentration level. The distinct Raman mode at 722 cm^{-1} delivers linear dependence on log intensity versus analyte at lower concentrations and shows higher R^2 value of 0.99; the details are shown in Figure 12B. Another DNA base as cytosine has also been detected with AgNDs@AuNPs-3 substrate. Cytosine is one of the sequences of four DNA bases that can encode the genetic instructions of human cells. The sensitivity of cytosine was examined with different solutions (1 mM–10 nM concentration range), and the SERS spectra are shown in Figure 12C. The characteristic vibrational peaks of cytosine were indexed at 604 cm^{-1}, 792 cm^{-1}, 1115 cm^{-1}, 1251 cm^{-1}, 1368 cm^{-1}, 1524 cm^{-1}, 1641 cm^{-1}, and the corresponding vibrations are shown in Table S2 (Madzharova et al., 2016). The intensity of a specific mode at 792 cm^{-1} shows a signature peak even at lower-level detection, which proves that the AuNPs composed AgNDs play a significant role in biomarker detection. The associated log intensity versus analyte at lower concentration plot produced linearity with an effective R^2 of 0.99, as shown in Figure 12D. The AEF at different concentrations of adenine and cytosine are shown in Table 1. Specifically, the AEF of 100 nM adenine, 10 nM cytosine were estimated to be 1.7×10^6, 8.1×10^6, respectively.

In sequential molecular detection, we have focused on antibiotics, which are proficient in preventing and treating infections in humans and animals (Wali et al., 2019; Chen et al., 2017). The abnormal utilization of

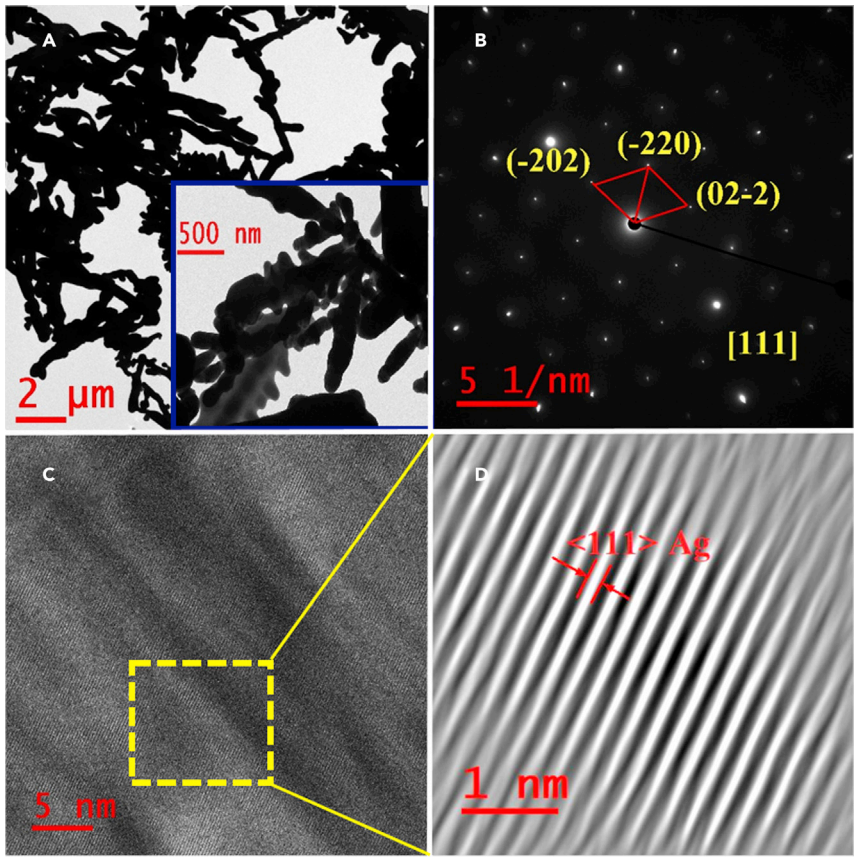

Figure 9. TEM images of AuNDs

(A) TEM image of AgNDs (inset depicts the higher magnification of the same image), (B) SAED pattern, (C) HRTEM image and the red dotted rectangular line indicates the area of selection for IFFT, and (D) IFFT data obtained from HRTEM image.

antibiotics causes bioaccumulation in water, animal food, and the environment, which is one of the widespread problems to be solved. As a part of the solution, SERS activity has been considered to be a reliable technique in the importance of antibiotic detection. In the present research, we mainly focused on detecting various antibiotics such as penicillin-G, kanamycin, and ampicillin. Firstly, the derivatives of penicillin-G have been considered for detection with concentrations ranging from 1 mM to 10 nM. The intensity discrimination of penicillin-G as a function of analyte concentration is shown in Figure 13A. The leading bands of penicillin-G are located at 985 cm^{-1}, 1586 cm^{-1}, and 1668 cm^{-1}, and the corresponding mode assignments are shown in Table S2 (Wali et al., 2019; Chen et al., 2017). The tracing of penicillin molecules at 10 nM concentration has also been noticed by observing the characteristic peaks at 985 cm^{-1}. These observations support the AuNPs composed of NDs possessing superior detection abilities. The linearity dependence was extracted by plotting the log intensity versus log concentration depicted an R^2 of 0.97, as shown in Figure 13B. Another essential antibiotic, kanamycin has also been considered for detection because the residual amount of kanamycin in clinical cases causes serious side effects such as loss of hearing, allergy reactions, and foodstuff leading to pathogenic-bacterial strains (Zengin et al., 2014; Jiang et al., 2020). The ability to detect at various concentrations (1 mM–100 nM) of kanamycin is shown in Figure 13C data. The signature peak at 975 cm^{-1} has been detected at the lowest concentration of 100 nM of kanamycin. The linear dependence was confirmed by log intensity versus concentration plot with the linear fitting with an R^2 value of 0.98. The data and the fit are shown in Figure 13D. In the end, we focused on estimating these substrates' sensitivity toward ampicillin antibiotic, which is enormously used in livestock production and bacterial infections. The illegal use may affect human health through food contamination. Figure 13E reports the intensity modulations of the Raman mode at 988 cm^{-1} at various concentrations of ampicillin

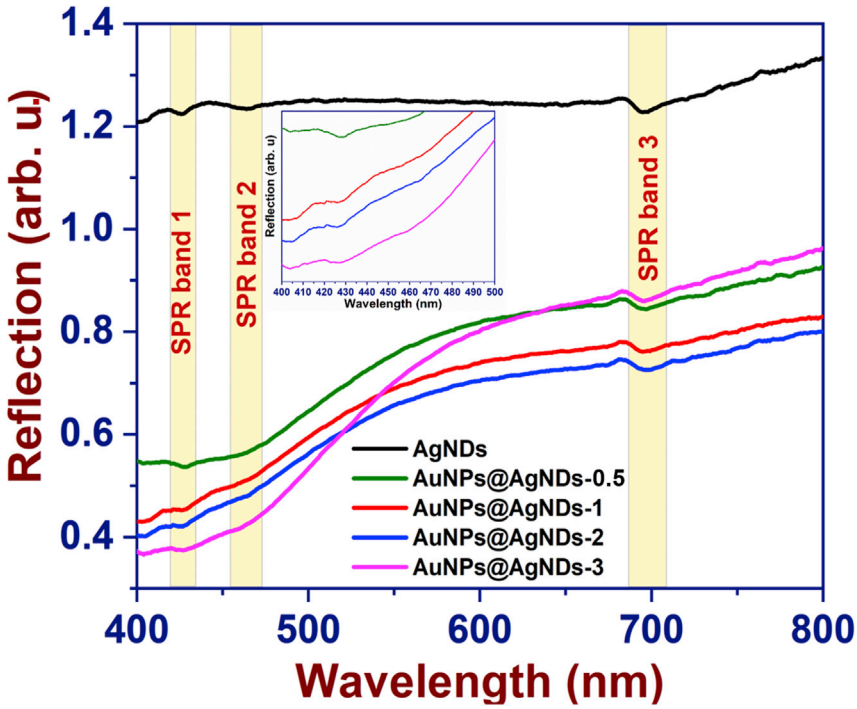

Figure 10. Reflectance spectra of AgNDs and AuNPs decorated AgNDs at various deposition times (inset shows the magnified SPR band one in 400–500 nm)

(varying from 1 mM to 10 nM). It is proved that the SERS-active substrate could detect 10 nM concentration in this case.

The linearity was extracted from the log-log plot at lower analyte concentration resulting in an R^2 of 0.98, and the data are shown in Figure 13F. The primary and essential parameter AEF was estimated for penicillin-G, kanamycin, and ampicillin as 5.4×10^6, 2.8×10^5, 7.2×10^6, for 10, 100, and 10 nM, respectively. The AEFs retrieved from the detailed studies at other concentrations are shown in Table 1. The uniquesensitivity and versatility of the substrate have been proved categorically for the detection of explosives and pesticides. This can extensively promote the importance and adaptability of AuNPs@AgNDs active substrates to investigate a wide variety of molecules. Ammonium nitrate is an explosive used as standard fertilizer and well exploited in defense. Also, it is critical in detection owing to its limited sensing ability and matrix properties. The sensitivity of the substrate was tested by introducing various concentrations of AN,

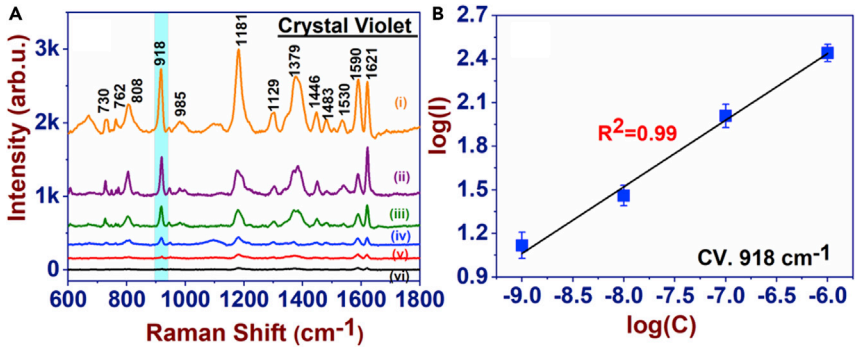

Figure 11. SERS spectra and mapping data of various analyte molecules

SERS spectra of CV (dye) on AuNPs@AgNDs-3 at (A) (i) 10 μM (ii) 5 μM (iii) 1 μM, and (iv)100 nM (v) 10 nM and (vi) 1 nM concentrations and (B) corresponding linear relationship of log (intensity) versus log (lower concentration) of the 918 cm^{-1} Raman peak. The error bars represent ±5% variation in the experimental values.

Table 1. Summary of estimated AEF and LOD for the detected analytes

Analyte molecules	Peak position (cm^{-1})	Concentration	Analytical enhancement factor (AEF)	LOD
Crystal violet	918	10 μM	2.1×10^{5}	348 pM
		5 μM	2.5×10^{5}	
		1 μM	6.8×10^{5}	
		100 nM	2.5×10^{6}	
		10 nM	7.1×10^{6}	
		1 nM	3.2×10^{7}	
Adenine	722	1 mM	2.1×10^{3}	2 nM
		100 μM	1.2×10^{4}	
		50 μM	1.7×10^{4}	
		10 μM	2.9×10^{4}	
		100 nM	1.7×10^{6}	
Cytosine	792	1 mM	2.2×10^{3}	28 nM
		100 μM	1.4×10^{4}	
		50 μM	2.2×10^{4}	
		10 μM	2.8×10^{4}	
		100 nM	2.1×10^{6}	
		10 nM	8.1×10^{6}	
Penicillin-G	985	1 mM	1.9×10^{3}	2 nM
		100 μM	1.7×10^{4}	
		50 μM	1.9×10^{4}	
		10 μM	3.2×10^{4}	
		100 nM	2.0×10^{6}	
		10 nM	5.4×10^{6}	
Kanamycin	975	1 mM	1.0×10^{3}	56 nM
		100 μM	5.1×10^{3}	
		50 μM	5.8×10^{3}	
		10 μM	9.1×10^{3}	
		100 nM	2.8×10^{5}	
Ampicillin	988	1 mM	1.1×10^{3}	4 nM
		100 μM	8.3×10^{3}	
		50 μM	1.2×10^{4}	
		10 μM	3.7×10^{4}	
		100 nM	1.7×10^{6}	
		10 nM	7.2×10^{6}	
Ammonium Nitrate	1045	50 μM	1.9×10^{4}	5 nM
		10 μM	6.3×10^{4}	
		5 μM	5.8×10^{4}	
		1 μM	1.7×10^{5}	
		100 nM	5.0×10^{5}	
Thiram	1384	10 μM	4.5×10^{3}	2 nM
		5 μM	5.8×10^{3}	
		300 nM	3.1×10^{4}	
		100 nM	2.3×10^{5}	
		10 nM	1.1×10^{6}	

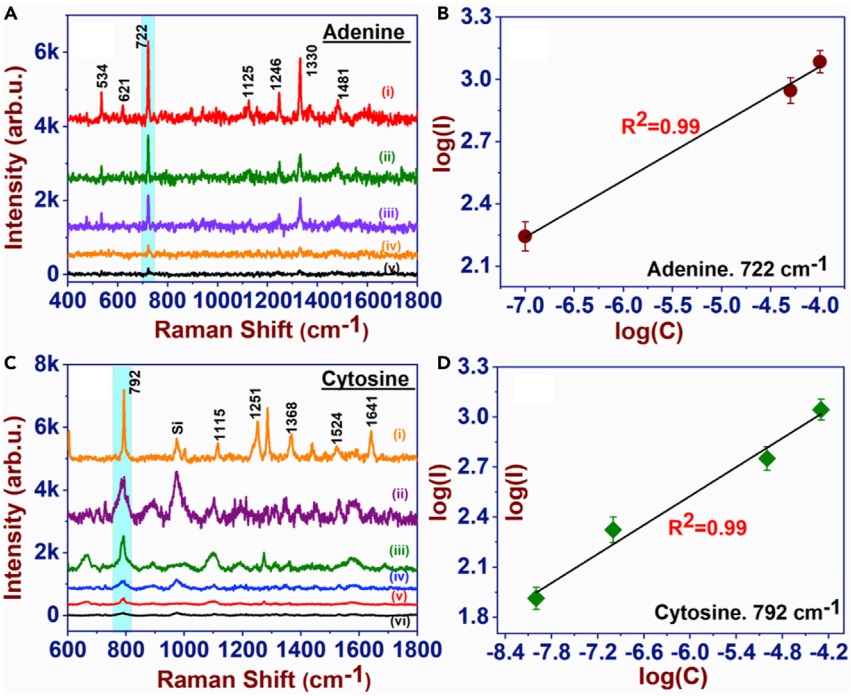

Figure 12. SERS spectra and mapping data of various analyte molecules

SERS spectra of adenine (DNA bases) on AuNPs@AgNDs-3 at (A) (i) 1 mM (ii) 100 μM (iii) 50 μM, and (iv)10 μM, and (v) 100 nM concentrations, (B) corresponding linear relationship of log (intensity) versus log (concentration) of the 722 cm^{-1} Raman peak, (C) Cytosine (i) 1 mM, (ii) 100 μM, (iii) 50 μM, and (iv) 10 μM M, (v) 100 nM, and (vi) 10 nM concentrations, and (D) corresponding linear relationship of log (intensity) versus log (concentration) of the 792 cm^{-1} Raman peak. The error bars represent ±4% variation in the experimental values.

ranging from 50 μM to 100 nM, as shown in Figure 14A. The observed Raman modes of AN at 711 cm^{-1} and 1045 cm^{-1} and the corresponding vibration assignments are shown in Table S2 (Zhou et al., 2021). It is keenly observed that the intensity of the signature peak at 1045 cm^{-1} changed predominantly as a function of analyte concentration which is shown in Figure 14A. The logarithmic plot of intensity versus analyte at lower concentrations demonstrated the linearity with R^2 of 0.99, as shown in Figure 14B. The calculated AEF for 100 nM concentration was ~5.0×10^5. Table 1 depicts the AEFs obtained at other concentrations of AN. From the SERS data presented and analyzed in our earlier work of AN (Vendamani et al., 2021) we conclude that the AuNPs@AgNDs-3 substrate produced an additional ~40% enhancement in the Raman intensity measured (10 μM) compared to the simple AgNDs. The observed significant intensity enhancement is owing to the higher stability (reduced natural oxidation effect) of AgNDs post-deposition of the AuNPs and also the cooperative (synergistic) effect of both AuNDs and AuNPs. The present studies have also been extended toward the detection of trace thiram, which is one of the common pesticides in food safety (Verma and Soni, 2019; Verma and Soni, 2021). The determination of substrate quality toward the thiram detection with a range of concentrations (10 μM–10 nM) was considered and the detailed data obtained are shown in Figure 15A. The Raman band assignments at 1140 cm^{-1}, 1385 cm^{-1}, and 1428 cm^{-1} and the corresponding assignments are shown in Table S2 (Bharati et al., 2019). The most prominent mode at 1385 cm^{-1} was noticed to be decreased with an increase in the concentration, and the data are presented in Figure 15A. A linear relation was investigated by a log plot of intensity versus concentration with 0.98 fitting accuracies, as shown in Figure 15B. Thiram with different concentrations was assessed by calculating the AEF shown in Table 1. At a definite 10 nM concentration of thiram, the AEF was estimated to be 1.1×10^6 for 10 nM concentration.

In addition to the SERS activity, sensitivity and reproducibility are indispensable factors in evaluating the final practical utility of the SERS substrate. To investigate the reproducibility of AuNPs@AgNDs substrate, signals of 5 μM CV and 50 μM cytosine were acquired at 10 random spots and the data are shown in

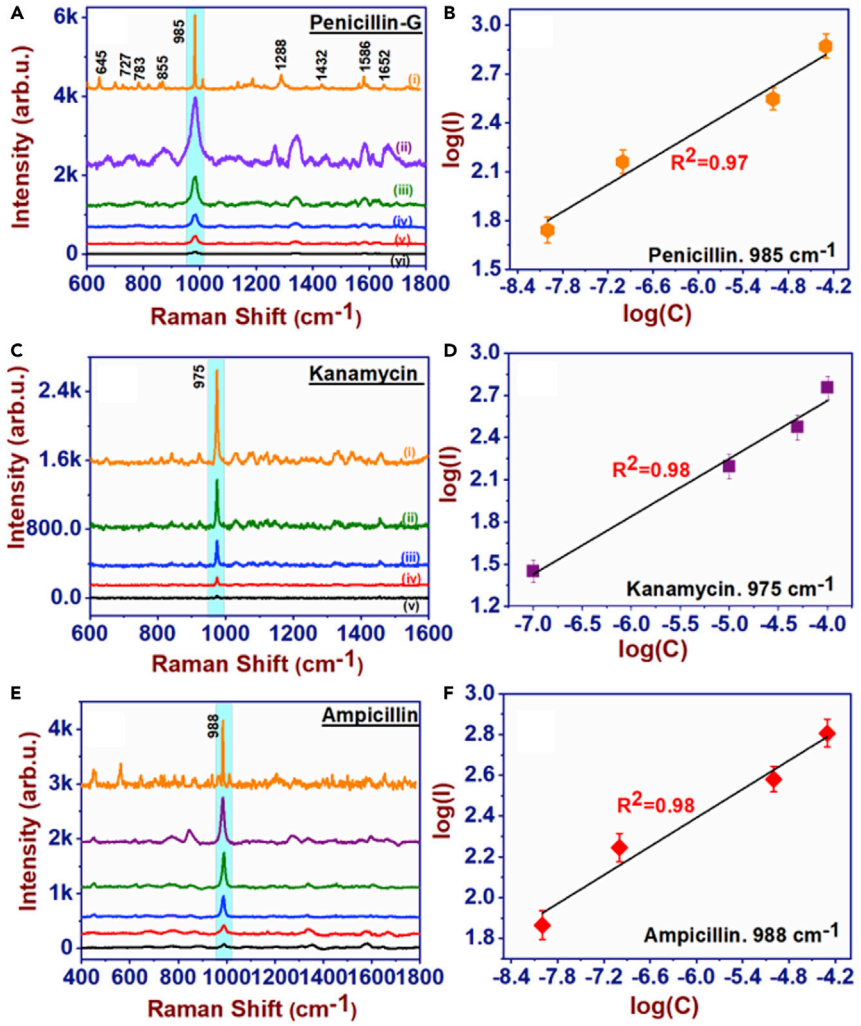

Figure 13. SERS spectra and mapping data of various analyte molecules

SERS spectra of penicillin G (antibiotic) on AuNPs@AgNDs-3 at (A) (i) 1 mM, (ii) 100 μM, (iii) 50 μM, and (iv) 10 μM M, (v) 100 nM, and (vi) 10 nM concentrations, and (B) corresponding linear relationship of log (intensity) versus log (concentration) of the 985 cm^{-1} Raman peak (C) Kanamycin (i) 1 mM, (ii) 100 μM, (iii) 50 μM, and (iv)10 μM, and (v) 100 nM concentrations, and (D) corresponding linear relationship of log (intensity) versus log (concentration) of the 975 cm^{-1} Raman peak, (E) Ampicillin (i) 1 mM, (ii) 100 μM, (iii) 50 μM, and (iv)10 μM, (v) 100 nM, and (vi) 10 nM concentrations, and (F) corresponding linear relationship of log (intensity) versus log (concentration) of the 988 cm^{-1} Raman peak. The error bars represent ±5% variation in the experimental values.

Figures 16A and 16B. The peak intensity distributions of 918 cm^{-1} and 792 cm^{-1} for CV and cytosine exhibited smaller deviations with RDS values of ~8%, and ~7%, respectively, in the bar graph shown in Figure 16C. The recently reported limit of deviation for various substrates was ~5%, suggesting that our substrates produced good signal reproducibility. However, there is scope for improvement through the optimization of the AuNPs sizes and distribution. Furthermore, in connection with reproducibility, time stability (meaning how much the substrate performance degrades over time) is also a significant aspect of judging the substrate quality and effectiveness. The sensitivity of the sample is examined by comparing the Raman signals of CV on AuNPs@AgNDs-3 substrate, which were exposed to ambient environment at different periods (i.e., 0, 10, 20, 30, 40, 50, 60, 70, 80, 90, 100, and 120 days). The data are shown in Figure 16D. It is noticed that distinctive intensity and position changes were not observed in the significant Raman peaks over the period of 4–5 weeks of exposure. Subsequently, the intensity of the Raman peak (918 cm^{-1}) decreased over time to ambient exposure. We had noticed characteristic peaks of the CV molecule even after 120 days of exposure. Based on the above data, we concluded that the combination of

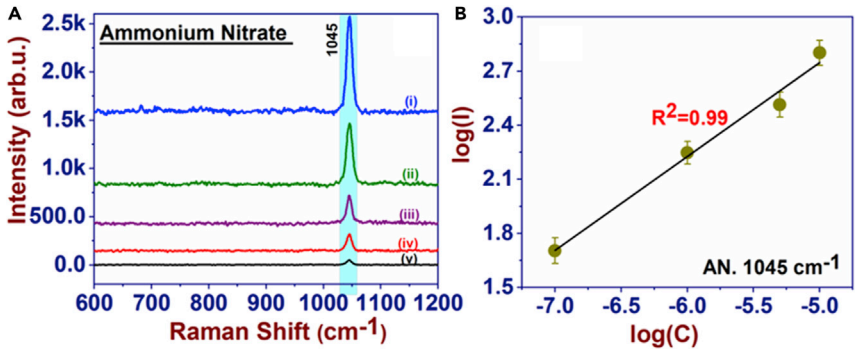

Figure 14. SERS spectra and mapping data of various analyte molecules

SERS spectra of AN (explosive) on AuNPs@AgNDs-3 at (A) (i) 50 μM, (ii) 10 μM, (iii) 5 μM, and (iv) 1 μM, and (v) 100 nM concentrations, and (B) corresponding linear relationship of log (intensity) versus log (concentration) of the 1045 cm^{-1} Raman peak. The error bars represent ±4% variation in the experimental values.

AgNSs and AuNSs promises better reproducibility and stability. Besides, we firmly believe that the stability can be improved further by storing the samples in a high vacuum immediately after preparation. Moreover, we are exploring the aspect of coating these substrates with 2D materials such as graphene, MoS_2 for additional enhancements (chemical) and stability that are a subject of our future studies.

The Raman mapping was performed with crystal violet (concentration of 1 μM) at a randomly chosen large area of 45 × 45 μm^2 with 4 μm spacing with 10× microscope objective. We collected nearly 120 SERS spectra on the sample using an inbuilt microscope for achieving the mapping and the data are shown in Figures 17A–17C. The RSD value of the 80 selected spectra (from Figure 17B mapping data) shown in Figure 17C was <5%. Similarly, the RSD value of the 170 selected spectra (from Figure 17B mapping data) shown in Figure 17C was <7%. The acquisition time was set to 3s with three spectra averaged at each point. Later, small area Raman mapping was also performed within an area of 20 × 20 μm^2 with a spacing of ~1.5 μm by collecting nearly 200 spectra. The SERS intensities across the mapping area are represented using color maps for Raman modes of CV 918 cm^{-1} corresponding to ring skeletal vibrations (Vendamani et al., 2020). The color scale indicates the intensity counts for each mode. The color maps show a homogeneous distribution for a large part except for small areas resembling islands in the whole mapping area. This can be attributed to a high density of hotspots in some regions of the sample owing to the distribution of AgNPs on the AgNDs and the overlapping of AgNDs as seen in the FESEM images (Figure 3). The signal variation can also be attributed to non-homogenous adsorption of the analyte on the substrate, orientation of the molecules, and coupling of the molecules with the nanoparticles and the laser, along with the distance between the molecules and the hotspot. It is pertinent to note here that the signal collection during the mapping was from a single plane and not from the highest signal plane of the substrate. These

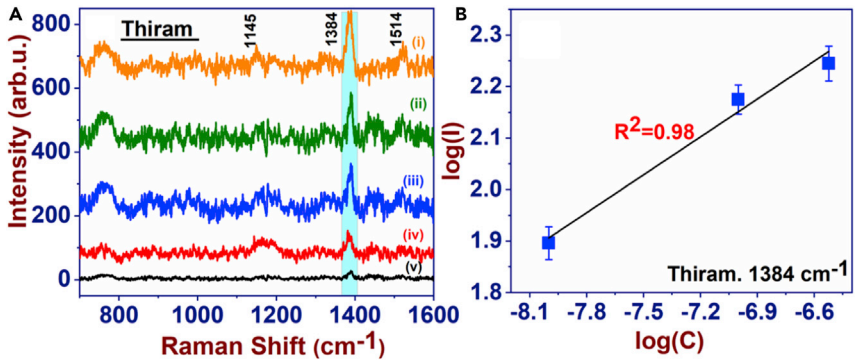

Figure 15. SERS spectra and mapping data of various analyte molecules

SERS spectra of thiram (pesticide) on AuNPs@AgNDs-3 at (A) (i) 10 μM (ii) 5 μM (iii) 300 nM (iv)100 nM and (v) 10 nM concentrations, and (B) corresponding linear relationship of log (intensity) versus log (concentration) of the 1384 cm^{-1} Raman peak. The error bars represent ±4% variation in the experimental values.

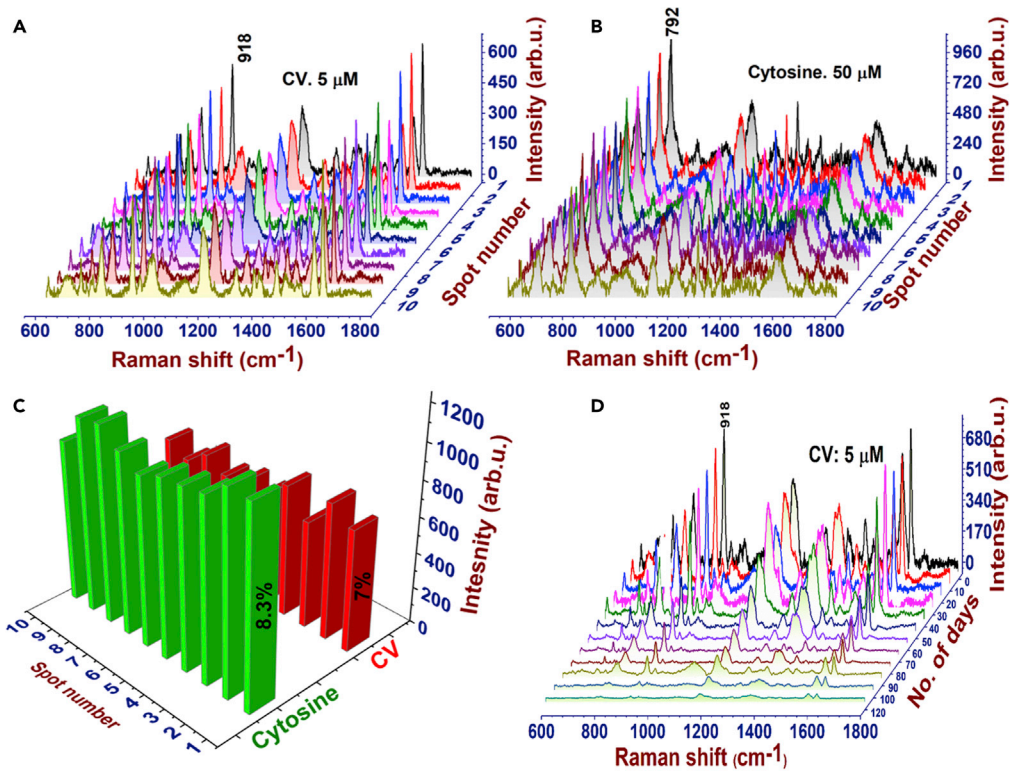

Figure 16. SERS spectra and mapping data of various analyte molecules

Spectral reproducibility of (A) CV at 5 μM, and (B) cytosine at 50 μM concentrations, (C) corresponding histogram with RSD values, (D) stability estimation of AuNPs@AgNDs-3 substrate at 5 μM CV over 120 days.

are three-dimensional anisotropic dendrites and the position of these dendrites along with the AuNPs determines the total Raman signal. Further improvements are possible if one uses an automated z axis scanning to autofocus combined with a small program to collect the best Raman signal from each point. This will certainly reduce the RSD value but increase the scanning time. Another aspect one can consider is to increase the enhancement factors by 3–4 times which will then render these relatively higher RSD values insignificant because the overall enhancements are much higher. The Raman signal deviation is, however, relatively less in small area mapping. Similar studies were carried out for cytosine of concentration 10 μM with 792 cm^{-1} peaks as mapping region with an area of 100 × 100 μm^2, 20 × 20 μm^2 as indicated in Figures 17D–17F. Figure 17A shows better reproducibility for CV with large area Raman mapping (40 × 40 μm^2). However, 20 × 20 μm^2 (Figure 17B) depicts a slightly inferior reproducibility because the spacing used during the mapping was 1.5 μm with a laser spot size of 2.6 μm. This means that there was an overlap of collection area throughout the region which could have led to photodegradation effects in the dye, thereby, decreasing the Raman signal. Figure 17F is the Raman mapping data of cytosine under the same conditions and exhibits a better reproducibility as opposed to the dye. Therefore, we believe that this low reproducibility for dye is possibly an attribute of laser-induced effects from the dye because of the overlap in the collection area.

To visualize near-field enhancement around the nanostructures fabricated in the present study, we have performed simulations using Comsol, shown in Figures 18A and 18B. Electromagnetic wave polarized in the X-direction and propagating in the Y-direction with 532 nm wavelength was used for excitation. The field maps indicate that the sharp edges of the silver dendrites offer a significant advantage by employing higher field enhancements through the lightning rod effect. Pentagon-shaped gold nanoparticles above these dendrites were added further and clearly, additional enhancement is shown in Figure 18B. We believe that these hybrid SERS substrates have strong potential for practical applications with additional optimization studies in terms of the sizes and density of the Au NPs on Ag NDs.

We have compared the detection capabilities of various Ag and Au-based SERS substrates with the present work, and the results are shown in Table S1. After considering all the listed substrates and

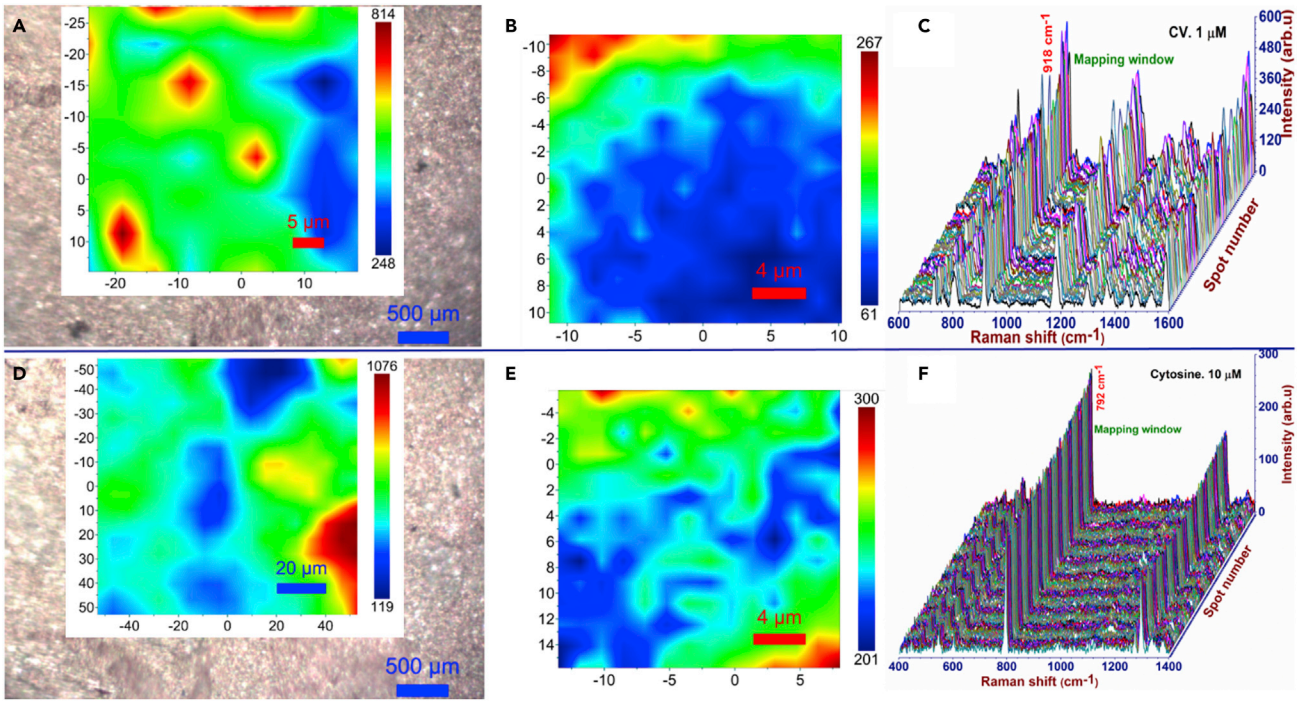

Figure 17. SERS spectra and mapping data of various analyte molecules

(A) Selected large-area Raman mapping (45 × 45 μm^2) of SERS substrate with 532×nm laser excitation, 10× microscope objective, 25 mW laser power with CV as probe molecule for 918 cm^{-1} Raman mode with 3s acquisition time, averaged over three spectra (B) Small area (20 × 20 μm^2) SERS mapping of CV (C) corresponding representative spectra of the mapping region, (D) Selected large-area Raman mapping (100 × 100 μm^2) - cytosine as probe molecule for the 792 cm^{-1} Raman mode (with similar acquisition parameters mentioned in (A)) (E) Small area (20 × 20 μm^2) SERS mapping of 10 μM cytosine (F) Corresponding representative spectra of the mapping region (presented in (E)). The background (gray color) in (A) and (D) depicts the optical microscope images of the substrates.

their data, we found that the SERS substrate synthesized in the current work demonstrated superior qualities to many of the recently reported ones. Besides the keen observation of SERS activity, the limit of detection (LOD) is an imperative parameter to justify the quality factor. The demonstrations of LOD calculation are shown in Figures S1–S5. In brief, the extracted LODs for all the molecules are shown in Table 1. The AEFs for other concentrations of molecules are reported in S1. In other words, the present demonstrations will be extensively promoted toward detecting other hazardous analytes and biomolecule mixtures. Additional challenging modifications such as incorporating 2D materials (i.e., graphene, MOS_2, and so forth) on these substrates will probably improve the molecular AEFs and stability further via synergetic effects.

Conclusions

It is reported that the combination of Au and Ag NSs shows tremendous effects on SERS sensing. Here we proposed an AuNPs decorated AgNDs for superior bimolecular detection. The density correlated with the Raman signal by controlling the AuNPs deposition time as 30 min, 1 h, 2 h, and 3 h. The biocompatible AuNPs@AgNDs-3 produced trace level detection in a wide range of molecules such as CV, DNA bases (adenine, cytosine), antibiotics (penicillin G, kanamycin, ampicillin), an explosive (AN), and a pesticide (thiram) molecule. The LODs obtained for CV, adenine, cytosine, penicillin G, kanamycin, ampicillin, AN, and thiram were 348 pM, 2, 28, 2, 56, 4, 5, and 2 nM, respectively. The sensitivity for each analyte was confirmed by assessing the analytical enhancement factor (AEF), which was ~10^7 for CV, ~10^6 for biomolecules, ~10^6 for explosive, and finally achieved ~10^6 for thiram. The spectral reproducibility was investigated and our data presented RSD values of 8 and 7% for CV and cytosine, respectively. The passivation of AuNPs over AgNDs promoted good stability over the period of 120 days of exposure. These robust, extremely low-cost substrates (when compared to some of the commercially available substrates (Bharati and Soma, 2021)) will be used for further investigations on the bimolecular mixtures.

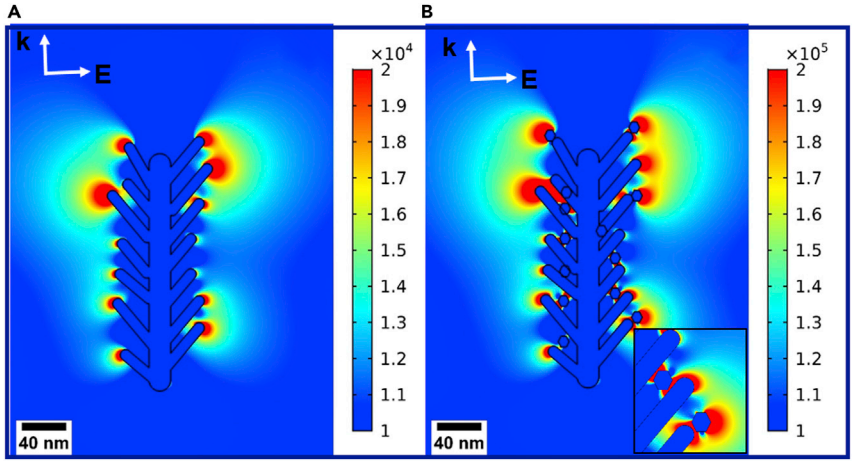

Figure 18. SERS spectra and mapping data of various analyte molecules

Near field maps simulated using COMSOL for (A) Ag dendrites (B) Ag dendrites with Au nanoparticles for electromagnetic wave polarized in the x-direction and propagating in the y-direction with 532 nm excitation (shows field enhancement around Au nanoparticle).

Limitations of the study

In the present report, the decoration of AuNPs on AgNDs was achieved by a simple electro-less deposition approach. The effect of various dimensional AuNSs on AgNDs is huge and the complete studies on different sized AuNSs decorated on AgNDs will be studied later and an understanding of the underlying effects on Raman enhancements will be explored. The SERS technique has been used to diagnose the molecules at trace level concentrations. However, there is future scope for investigating the mixtures of biomolecules and explosive molecules.

STAR★METHODS

Detailed methods are provided in the online version of this paper and include the following:

- KEY RESOURCES TABLE
- RESOURCE AVAILABILITY
  - Lead contact
  - Materials availability
  - Date and code availability
- METHOD DETAILS
  - Silver nano-dendrite formation
  - Gold nanoparticle decoration
  - Characterization techniques
  - Simulation methods
  - Surface enhanced Raman spectroscopy
- QUANTIFICATION AND STATISTICAL ANALYSIS

SUPPLEMENTAL INFORMATION

Supplemental information can be found online at https://doi.org/10.1016/j.isci.2022.104849.

ACKNOWLEDGMENTS

VSV thanks UGC, New Delhi, for fellowship in the form of DS Kothari postdoctoral fellowship (sanction order no. F.4–2/2006 (BSR)/PH/19–20/0008). We acknowledge Prof. V.V. Ravi Kanth Kumar, Department of Physics, Pondicherry University for his support and help in the analysis and measurement of XPS. V.R. Soma thanks DRDO, India for financial support (# ERIP/ER/1501138/M/01/319/D (R&D)). V.R. Soma and S.V.S.N. Rao thank the University of Hyderabad (UoH) for financial support from the Institute of Eminence (IoE) with a project (No. UOH/IOE/RC1/RC1-20-016). The IoE scheme was granted to the University by the

Ministry of Education, Government of India, vide MHRD notification F11/9/2019-U3(A). S. V. Rao thanks Director, ACRHEM, and Dr. Bikash Ghose, HEMRL for their support and encouragement during various discussions.

AUTHOR CONTRIBUTIONS

VSV planned the work, prepared the samples, carried out the Raman and other characteristic investigations, and wrote the original draft. RB performed the Raman mapping and COMSOL simulations. MMN helped with XPS measurements and analysis of the data. SVSNR provided an idea on conceptualization, reviewed, and edited the article. VRS conceived the project idea, conceptualized, supervised this work, corrected the original draft, and provided funding support.

DECLARATION OF INTERESTS

The authors declare that they have no known competing financial interests or personal relationships that could have appeared to influence the work reported in this article.

Received: May 6, 2022
Revised: June 15, 2022
Accepted: July 22, 2022
Published: August 19, 2022

REFERENCES

Amiens, C., Ciuculescu-Pradines, D., and Philippot, K. (2016). Controlled metal nanostructures: fertile ground for coordination chemists. Coord. Chem. Rev. *308*, 409–432.

Agustina, T.E., Handayani, W., and Imawan, C. (2020). The UV-VIS spectrum analysis from silver nanoparticles synthesized using Diospyros maritima blume. Leaves extract. Adv. Biol. Sci. Res. *14*, 411–419.

Bandarenka, H.V., Khinevich, N.V., Burko, A.A., Redko, S.V., Zavatski, S.A., Shapel, U.A., Mamatkulov, K.Z., Vorobyeva, M.Y., and Arzumanyan, G.M. (2020). 3D silver dendrites for single-molecule imaging by surface-enhanced Raman spectroscopy. ChemNanoMat *7*, 141–149.

Banerjee, D., Akkanaboina, M., Ghosh, S., and Soma, V.R. (2022). Picosecond bessel beam fabricated pure, gold-coated silver nanostructures for trace-level sensing of multiple explosives and hazardous molecules. Materials *15*, 4155.

Barbillon, G. (2020). Application of novel plasmonic nanomaterials on SERS. Nanomaterials *10*, 2308.

Beeram, R., Banerjee, D., Narlagiri, L.M., and Soma, V.R. (2022). Machine learning for rapid quantification of trace analyte molecules using SERS and flexible plasmonic paper substrates. Anal. Methods *14*, 1788–1796.

Bharati, M.S.S., Byram, C., and Soma, V.R. (2018). Femtosecond laser fabricated Ag@Au and Cu@Au alloy nanoparticles for surface enhanced Raman spectroscopy based trace explosives detection. Front. Phys. *6*, 28. https://doi.org/10.3389/fphy.2018.00028.

Bharati, M.S.S., Chandu, B., and Rao, S.V. (2019). Explosives sensing using Ag–Cu alloy nanoparticles synthesized by femtosecond laser ablation and irradiation. RSC Adv. *9*, 1517–1525.

Bharati, M.S.S., and Soma, V.R. (2021). Flexible SERS substrates for hazardous materials detection: recent advances. Opto-Electronic Adv. *4* (12), 210048.

Bijanzadeh, A.R., Vakili, M.R., and Khordad, R. (2012). A study of the surface plasmon absorption band for nanoparticles. Int. J. Phys. Sci. *7*, 1943–1948.

Bora, T. (2018). Recent developments on metal nanoparticles for SERS applications. Noble and Precious Metals - Properties, Nanoscale Effects and Applications6 (Intech Open), pp. 117–135. https://doi.org/10.5772/intechopen.71573.

Bremer, M.T., and Dantus, M. (2013). Standoff explosives trace detection and imaging by selective stimulated Raman scattering. Appl. Phys. Lett. *103*, 061119.

Burda, C., Chen, X., Narayanan, R., and El-Sayed, M.A. (2005). Chemistry and properties of nanocrystals of different shapes. Chem. Rev. *105*, 1025–1102.

Byram, C., Moram, S.S.B., and Soma, V.R. (2019). SERS based detection of multiple analytes from dye/explosive mixtures using picosecond laser fabricated gold nanoparticles and nanostructures. Analyst *144*, 2327–2336.

Ceballos, M., López, I., Arizmendi-Morquecho, A., and Sánchez-Domínguez, M. (2022). Attomolar detection of 4-aminothiophenol by SERS using silver nanodendrites decorated with gold nanoparticles. Nanotechnology *33*, 385602.

Chaudhari, K., Ahuja, T., Murugesan, V., Subramanian, V., Ganayee, M.A., Thundat, T., and Pradeep, T. (2018). Appearance of SERS activity in single silver nanoparticles by laser-induced reshaping. Nanoscale *11*, 321–330.

Chen, Y., Li, X., Yang, M., Yang, L., Han, X., Jiang, X., and Zhao, B. (2017). High sensitive detection of penicillin G residues in milk by surface-enhanced Raman scattering. Talanta *167*, 236–241.

Cheng, Z., Qiu, Y., Li, Z., Yang, D., Ding, S., Cheng, G., Hao, Z., and Wang, Q. (2019a). Fabrication of silver dendrite fractal structures for enhanced second harmonic generation and surface-enhanced Raman scattering. Opt. Mater. Express *9*, 860–868.

Cheng, Z.Q., Li, Z.W., Xu, J.H., Yao, R., Li, Z.L., Liang, S., Cheng, G.L., Zhou, Y.H., Luo, X., and Zhong, J. (2019b). Morphology-Controlled fabrication of large-scale dendritic silver nanostructures for catalysis and SERS applications. Nanoscale Res. Lett. *14*, 89.

Cheng, Z.Q., Li, Z.L., Luo, X., Shi, H.Q., Luo, C.L., Liu, Z.M., and Nan, F. (2019c). Enhanced second harmonic generation by double plasmon resonances in mesoscale flower-like silver particles. Appl. Phys. Lett. *114*, 011901.

Cheng, Z.Q., Li, Z.W., Yao, R., Xiong, K.W., Cheng, G.L., Zhou, Y.H., Luo, X., and Liu, Z.M. (2020). Improved SERS performance and catalytic activity of dendritic Au/Ag bimetallic nanostructures based on Ag dendrites. Nanoscale Res. Lett. *15*, 117.

Dubey, A., Mishra, R., Cheng, C.W., Kuang, Y.P., Gwo, S., and Yen, T.J. (2021). Demonstration of a superior deep-UV surface-enhanced resonance Raman scattering (SERRS) substrate and single-base mutation detection in oligonucleotides. J. Am. Chem. Soc. *143*, 19282–19286.

Fateixa, S., Nogueira, H.I.S., and Trindade, T. (2018). Surface-enhanced Raman scattering spectral imaging for the attomolar range detection of crystal violet in contaminated water. ACS Omega *3*, 4331–4341.

Fleischmann, M., Hendra, P.J., and Mcquillan, A.J. (1974). Raman spectra of pyridzne adsorbed at a silver electrode. Chem. Phys. Lett. *26*, 163–166.

Gu, H.X., Xue, L., Zhang, Y.F., Li, D.W., and Long, Y.T. (2015). Facile fabrication of a silver dendrite-integrated chip for surface-enhanced Raman scattering. ACS Appl. Mater. Interfaces *7*, 2931–2936.

Gutés, A., Carraro, C., and Maboudian, R. (2011). Ultrasmooth gold thin films by self-limiting galvanic displacement on silicon. ACS Appl. Mater. Interfaces *3*, 1581–1584.

Gutés, A., Maboudian, R., and Carraro, C. (2012). Gold-coated silver dendrites as SERS substrates with an improved lifetime. Langmuir *28*, 17846–17850.

Hamad, S., Podagatlapalli, G.K., Mohiddon, M.A., and Soma, V.R. (2014). Cost effective nanostructured copper substrates prepared with ultrafast laser pulses for explosives detection using surface enhanced Raman scattering. Appl. Phys. Lett. *104*, 263104.

Hashemi, F.S.M., Grillo, F., Ravikumar, V.R., Benz, D., Shekhar, A., Griffiths, M.B.E., Barry, S.T., and van Ommen, J.R. (2020). Thermal atomic layer deposition of gold nanoparticles: controlled growth and size selection for photocatalysis. Nanoscale *12*, 9005–9013.

Hatakeyama, Y., Onishi, K., and Nishikawa, K. (2011). Effects of sputtering conditions on formation of gold nanoparticles in sputter deposition technique. RSC Adv. *1*, 1815–1821.

Huang, J., Ma, D., Chen, F., Bai, M., Xu, K., and Zhao, Y. (2015a). Ag nanoparticles decorated cactus-like Ag dendrites/Si nanoneedles as highly efficient 3D surface-enhanced Raman scattering substrates toward sensitive sensing. Anal. Chem. *87*, 10527–10534.

Huang, J., Zhu, Y., Liu, C., Zhao, Y., Liu, Z., Hedhili, M.N., Fratalocchi, A., and Han, Y. (2015b). Fabricating a homogeneously alloyed AuAg Shell on au nanorods to achieve strong, stable, and tunable surface plasmon resonances. Small *11*, 5214–5221.

Jiang, T., Wang, X., Tang, S., Zhou, J., Gu, C., and Tang, J. (2017). Seed-mediated synthesis and SERS performance of graphene oxide-wrapped Ag nanomushroom. Sci. Rep. *7*, 9795.

Jiang, Y., Sun, D.-W., Pu, H., and Wei, Q. (2019). Ultrasensitive analysis of kanamycin residue in milk by SERS-based aptasensor. Talanta *197*, 151–158.

Jiang, Y., Sun, D.-W., Pu, H., and Wei, Q. (2020). A simple and sensitive aptasensor based on SERS for trace analysis of kanamycin in milk. Food Measure. *14*, 3184–3193.

Johnson, P.B., and Christy, R.W. (1972). Optical constants of the noble metals. Phys. Rev. B *6*, 4370–4379.

Kelly, K.L., Coronado, E., Zhao, L.L., and Schatz, G.C. (2003). The optical properties of metal nanoparticles: the influence of size, shape, and dielectric environment. J. Phys. Chem. B *107*, 668–677.

Khaywah, M.Y., Jradi, S., Louarn, G., Lacroute, Y., Toufaily, J., Hamieh, T., and Adam, P.M. (2015). Ultrastable, uniform, reproducible, and highly sensitive bimetallic nanoparticles as reliable large scale SERS substrates. J. Phys. Chem. C *119*, 26091–26100.

Kim, Y.T., Schilling, J., Schweizer, S.L., and Wehrspohn, R.B. (2017). High density ag nanobranches decorated with sputtered au nanoparticles for surfaceenhanced Raman spectroscopy. Appl. Surf. Sci. *410*, 525–529.

Kuntyi, O.I., Zozulya, G.I., Shepida, M.V., and Nichkalo, S.I. (2019). Deposition of nanostructured metals on the surface of silicon by galvanic replacement: a mini-review. Vopr. Khimii Khimicheskoi Tekhnologii *3*, 74–82. ISSN 0321-4095.

Li, H., Xu, B., Wang, D., Zhou, Y., Zhang, H., Xia, W., Xu, S., and Li, Y. (2015). Immunosensor for trace penicillin G detection in milk based on supported bilayer lipid membrane modified with gold nanoparticles. J. Biotechnol. *203*, 97–103.

Li, H.B., Liu, P., Liang, Y., Xiao, J., and Yang, G.W. (2012). Super-SERS-active and highly effective antimicrobial Ag nanodendrites. Nanoscale *4*, 5082–5091.

Li, L., Niu, R., and Zhang, Y. (2018). Ag–Au bimetallic nanocomposites stabilized with organic–inorganic hybrid microgels: synthesis and their regulated optical and catalytic properties. RSC Adv. *8*, 12428–12438.

Lirio, S., Liu, W.L., Lin, C.L., Lin, C.H., and Huang, H.Y. (2016). Aluminum based metal-organic framework-polymer monolith in solid-phase microextraction of penicillins in river water and milk samples. J. Chromatogr. A *1428*, 236–245.

Lo Faro, M.J., D'Andrea, C., Leonardi, A.A., Morganti, D., Irrera, A., and Fazio, B. (2019). Fractal silver dendrites as 3D SERS platform for highly sensitive detection of biomolecules in hydration conditions. Nanomaterials *9*, 1630.

Ma, J., Liu, X., Wang, R., Zhang, J., Jiang, P., Wang, Y., and Tu, G. (2020). Bimetallic core–shell nanostars with tunable surface plasmon resonance for surface-enhanced Raman scattering. ACS Appl. Nano Mater. *3*, 10885–10894.

Madzharova, F., Heiner, Z., Gühlke, M., and Kneipp, J. (2016). Surface-enhanced hyper-Raman spectra of adenine, guanine, cytosine, thymine, and uracil. J. Phys. Chem. C Nanomater. Interfaces *120*, 15415–15423.

Magagnin, L., Bertani, V., Cavallotti, P.L., Maboudian, R., and Carraro, C. (2002). Selective deposition of gold nanoclusters on silicon by a galvanic displacement process. Microelectron. Eng. *64*, 479–485.

Moram, S.S.B., Byram, C., Shibu, S.N., Chilukamarri, B.M., and Soma, V.R. (2018). Ag/Au nanoparticle-loaded paper-based versatile surface-enhanced Raman spectroscopy substrates for multiple explosives detection. ACS Omega *3*, 8190–8201.

Ngan, L.T.Q., Minh, K.N., Cao, D.T., Anh, C.T., and Van Vu, L. (2017). Synthesis of silver nanodendrites on silicon and its application for the trace detection of pyridaben pesticide using surface-enhanced Raman spectroscopy. J. Electron. Mater. *46*, 3770–3775.

Ouyang, H., Ling, S., Liang, A., and Jiang, Z. (2018). A facile aptamer-regulating gold nanoplasmonic SERS detection strategy for trace lead ions. Sensor. Actuator. B Chem. *258*, 739–744.

Palazzo, G., Valenza, G., Dell'Aglio, M., and De Giacomo, A. (2017). On the stability of gold nanoparticles synthesized by laser ablation in liquids. J. Colloid Interface Sci. *489*, 47–56.

Pastorello, M., Sigoli, F.A., Dos Santos, D.P., and Mazali, I.O. (2020). On the use of Au@Ag core-shell nanorods for SERS detection of Thiram diluted solutions. Spectrochim. Acta Mol. Biomol. Spectrosc. *231*, 118113.

Podagatlapalli, G.K., Hamad, S., and Rao, S.V. (2015). Trace-level detection of secondary explosives using hybrid silver–gold nanoparticles and nanostructures achieved with femtosecond laser ablation. J. Phys. Chem. C *119*, 16972–16983.

Portnov, A., Rosenwaks, S., and Bar, I. (2008). Detection of particles of explosives via backward coherent anti-Stokes Raman spectroscopy. Appl. Phys. Lett. *93*, 041115.

Powell, J.A., Venkatakrishnan, K., and Tan, B. (2017). Toward universal SERS detection of disease signaling bioanalytes using 3D self-assembled nonplasmonic near-quantum-scale silicon probe. ACS Appl. Mater. Interfaces *9*, 40127–40142.

Rao, V.K., and Radhakrishnan, T.P. (2015). Tuning the SERS response with Ag-Au nanoparticle-embedded polymer thin film substrates. ACS Appl. Mater. Interfaces *7*, 12767–12773.

Rathod, J., Byram, C., Kanaka, R.K., Sree Satya Bharati, M., Banerjee, D., Akkanaboina, M., and Soma, V.R. (2022). Hybrid surface-enhanced Raman scattering substrates for the trace detection of ammonium nitrate, thiram, and nile blue. ACS Omega *7*, 15969–15981.

Ravi Kumar, K., Jagannath, R., Vendamani, V.S., Pathak, A.P., Nageswara Rao, S.V.S., and Venugopal Rao, S. (2021). Gold nanostars on porous silicon for sensing picric acid, malachite green using SERS. Proc. SPIE *11869*, 1186904.

Samal, A.K., Polavarapu, L., Rodal-Cedeira, S., Liz-Marzán, L.M., Pérez-Juste, J., and Pastoriza-Santos, I. (2013). Size tunable Au@Ag core-shell nanoparticles: synthesis and surface-enhanced Raman scattering properties. Langmuir *29*, 15076–15082.

Shaik, U.P., Hamad, S., Ahamad Mohiddon, M., Soma, V.R., and Ghanashyam Krishna, M. (2016). Morphologically manipulated Ag/ZnO nano-structures as surface enhanced Raman scattering probes for explosives detection. J. Appl. Phys. *119*, 093103. https://doi.org/10.1063/1.4943034.

Shen, J., Su, J., Yan, J., Zhao, B., Wang, D., Wang, S., Li, K., Liu, M., He, Y., Mathur, S., et al. (2014). Bimetallic nano-mushrooms with DNA-mediated interior nanogaps for high-efficiency SERS signal amplification. Nano Res. *8*, 731–742.

Shepida, M., Kuntyi, O., Nichkalo, S., Zozulya, G., and Korniy, S. (2019). Deposition of gold nanoparticles via galvanic replacement in DMSO and their influence on formation of silicon nanostructures. Adv. Mater. Sci. Eng. *2019*, 1–7.

Srikanth, C.K., and Jeevanandam, P. (2012). Comparison of galvanic displacement and electroless methods for deposition of gold nanoparticles on synthetic calcite. Bull. Mater. Sci. *35*, 939–946.

Sun, W., Hong, R., Liu, Q., Li, Z., Shi, J., Tao, C., and Zhang, D. (2019). SERS-active Ag–Al alloy nanoparticles with tunable surface plasmon resonance induced by laser ablation. Opt. Mater. *96*, 109298.

Tao, A.R., and Yang, P. (2005). Polarized surface-enhanced Raman spectroscopy on coupled metallic nanowires. J. Phys. Chem. B *109*, 15687–15690.

Tian, Y., Liu, H., Chen, Y., Zhou, C., Jiang, Y., Gu, C., Jiang, T., and Zhou, J. (2019). Seedless one-spot synthesis of 3D and 2D Ag nanoflowers for multiple phase SERS-based molecule detection. Sensor. Actuator. B Chem. *301*, 127142.

Tim, B., Błaszkiewicz, P., and Kotkowiak, M. (2021). Recent advances in metallic nanoparticle assemblies for surface-enhanced spectroscopy. Int. J. Mol. Sci. *23*, 291.

Tzeng, Y., and Lin, B.Y. (2020). Silver-based SERS pico-molar adenine sensor. Biosensors *10*, 122.

Velázquez-Salazar, J.J., Bazán-Díaz, L., Zhang, Q., Mendoza-Cruz, R., Montaño-Priede, L., Guisbiers, G., Large, N., Link, S., and José-Yacamán, M. (2019). Controlled overgrowth of five-fold concave nanoparticles into plasmonic nanostars and their single-particle scattering properties. ACS Nano *13*, 10113–10128.

Vendamani, V.S., Chandu, B., Venugopal Rao, S., Kanjilal, D., Pathak, A.P., and Nageswara Rao, S.V.S. (2018a). Metal nanoparticle encompassed nanostructured porous silicon for effective molecular detection based on SERS proc. Photonics. In 2018, International Conference on Fiber Optics and Photonics, Paper # SP133978-93-88653-41-1.

Vendamani, V.S., Nageswara Rao, S.V.S., Venugopal Rao, S., Kanjilal, D., and Pathak, A.P. (2018b). Three-dimensional hybrid silicon nanostructures for surface enhanced Raman spectroscopy based molecular detection. J. Appl. Phys. *123*, 014301.

Vendamani, V.S., Rao, S.V.S.N., Pathak, A.P., and Soma, V.R. (2020). Robust and cost-effective silver dendritic nanostructures for SERS-based trace detection of RDX and ammonium nitrate. RSC Adv. *10*, 44747–44755.

Vendamani, V.S., Beeram, R., Nageswara Rao, S.V.S., Pathak, A.P., and Soma, V.R. (2021). Trace level detection of explosives and pesticides using robust, low-cost, free-standing silver nanoparticles decorated porous silicon. Opt Express *29*, 30045–30061.

Vendamani, V.S., Rao, S.V.S.N., Pathak, A.P., and Soma, V.R. (2022). Silicon nanostructures for molecular sensing: a review. ACS Appl. Nano Mater. *5*, 4550–4582.

Verma, A.K., and Soni, R.K. (2019). Silver nanodendrites for ultralow detection of thiram based on surface-enhanced Raman spectroscopy. Nanotechnology *30*, 385502.

Verma, A.K., and Soni, R.K. (2021). Multi-spiked silver stars for ultrasensitive and multiplexed SERS detection of analytes. J. Phys. D Appl. Phys. *54*, 475107.

Verma, A.K., and Soni, R.K. (2022). Ultrasensitive surface-enhanced Raman spectroscopy detection of explosive molecules with multibranched silver nanostructures. J. Raman Spectrosc. *53*, 694–708.

Wali, L.A., Hasan, K.K., and Alwan, A.M. (2019). Rapid and highly efficient detection of ultra-low concentration of penicillin G by gold nanoparticles/porous silicon SERS active substrate. Spectrochim. Acta Mol. Biomol. Spectrosc. *206*, 31–36.

Wang, X., Liu, C., Gao, C., Yao, K., Masouleh, S.S.M., Berté, R., Ren, H., Menezes, L.d.S., Cortés, E., Bicket, I.C., et al. (2021). Self-constructed multiple plasmonic hotspots on an individual fractal to amplify broadband hot electron generation. ACS Nano *15*, 10553–10564.

Weakliem, H.A., and Redfield, D. (1979). Temperature dependence of the optical properties of silicon. J. Appl. Phys. *50*, 1491–1493.

Wei, C., Li, M., and Zhao, X. (2018). Surface-enhanced Raman scattering (SERS) with silver nano substrates synthesized by microwave for rapid detection of foodborne pathogens. Front. Microbiol. *9*, 2857.

Wu, X., Xu, C., Tripp, R.A., Huang, Y.W., and Zhao, Y. (2013). Detection and differentiation of foodborne pathogenic bacteria in mung bean sprouts using field deployable label-free SERS devices. Analyst *138*, 3005–3012.

Xu, K.X., Guo, M.H., Huang, Y.P., Li, X.D., and Sun, J.J. (2018). Rapid and sensitive detection of malachite green in aquaculture water by electrochemical preconcentration and surface-enhanced Raman scattering. Talanta *180*, 383–388.

Yakimchuk, D.V., Kaniukov, E.Y., Lepeshov, S., Bundyukova, V.D., Demyanov, S.E., Arzumanyanm, G.M., Doroshkevich, N.V., Mamatkulov, K.Z., Bochmann, A., Presselt, M., et al. (2019). Self-organized spatially separated silver 3D dendrites as efficient plasmonic nanostructures for surface-enhanced Raman spectroscopy applications. J. Appl. Phys. *126*, 233105.

Yang, S., Dai, X., Stogin, B.B., and Wong, T.S. (2016). Ultrasensitive surface-enhanced Raman scattering detection in common fluids. Proc. Natl. Acad. Sci. USA *113*, 268–273.

Yin, H.J., Chen, Z.Y., Zhao, Y.M., Lv, M.Y., Shi, C.A., Wu, Z.L., Zhang, X., Liu, L., Wang, M.L., and Xu, H.J. (2015). Ag@Au core-shell dendrites: a stable, reusable and sensitive surface enhanced Raman scattering substrate. Sci. Rep. *5*, 14502.

Yu, X., Zhong, Y., Sun, Y., and Chen, Y. (2020). Controllable preparation of plasmonic gold nanostars for enhanced photothermal and SERS effects. Chem. Res. Chin. Univ. *36*, 1284–1291.

Zhang, C., Jiang, S.Z., Yang, C., Li, C.H., Huo, Y.Y., Liu, X.Y., Liu, A.H., Wei, Q., Gao, S.S., Gao, X.G., and Man, B.Y. (2016). Gold@silver bimetal nanoparticles/pyramidal silicon 3D substrate with high reproducibility for high-performance SERS. Sci. Rep. *6*, 25243.

Zhang, C.X., Su, L., Chan, Y.F., Wu, Z.L., Zhao, Y.M., Xu, H.J., and Sun, X.M. (2013). Ag@SiO2 core-shell nanoparticles on silicon nanowire arrays as ultrasensitive and ultrastable substrates for surface-enhanced Raman scattering. Nanotechnology *24*, 335501.

Zhang, Z., Liao, F., Ma, S., Gao, S., and Shao, M. (2015). SERS and FDTD simulation of gold nanoparticles grafted on germanium wafer via galvanic displacement. Surf. Interface Anal. *47*, 398–402.

Zhao, B., Lu, Y., Zhang, C., Fu, Y., Moeendarbari, S., Shelke, S.R., Liu, Y., and Hao, Y. (2016). Silver dendrites decorated filter membrane as highly sensitive and reproducible three dimensional surface enhanced Raman scattering substrates. Appl. Surf. Sci. *387*, 431–436.

Zengin, A., Tamer, U., and Caykara, T. (2014). Extremely sensitive sandwich assay of kanamycin using surface-enhanced Raman scattering of 2-mercaptobenzothiazole labeled gold@silver nanoparticles. Anal. Chim. Acta *817*, 33–41.

Zhou, H., Liang, Y., Zhang, J., and Wang, F. (2021). Detection of benzylpenicillin sodium and ampicillin residue based on flower-like silver nanostructures using surface-enhanced Raman spectroscopy. Res. Chem. Intermed. *48*, 117–128.

Zhu, H., Liu, S., Guo, Z., Yan, K., Shen, J., Zhang, Z., Chen, J., Guo, Y., Liu, L., and Wu, X. (2021). Strong histamine torsion Raman spectrum enables direct, rapid, and ultrasensitive detection of allergic diseases. iScience *24*, 103384.

STAR★METHODS

KEY RESOURCES TABLE

REAGENT or RESOURCE	SOURCE	IDENTIFIER
Chemicals, peptides, and recombinant proteins		
Silver salt ($AgNO_3$)	Finar, India	CAS No. 7783-90-6
Ethanol	Supelco, India	CAS No. 64-17-5
Hydrofluoric acid	Sigma-Aldrich, India	CAS No. 7664-39-3
$AuCl_4$:$3H_2O$	Sigma-Aldrich, India	CAS No. 16961-25-4
Antibiotics (Penicillin G, Kanamycin, Ampicillin)	Sigma-Aldrich, India	CAS No. 113-98-4; 64013-70-3; 7177-48-2
DNA bases (Adenine, Cytosine)	Sigma-Aldrich, India	CAS No. 73-24-5; 71-30-7
Ammonium Nitrate	HEMRL, Pune, India	NA
Thiram	Sigma-Aldrich, India	CAS No. 137-26-8
Software and algorithms		
Origin	www.originlab.com	Origin 2018
COMSOL	www.comsol.com	COMSOL 5.3
Gatan DM3	www.gatan.com	Gatan Microscopy Suite 3.x
Others		
Si wafers (1–10 Ω-cm, p-type)	Macwin India Ltd.	NA
Field emission scanning electron microscope	Carl ZEISS, Ultra 55	https://www.felmi-zfe.at/instrumentation/sem/zeiss-ultra-55/
Transmission electron microscope	Technai	https://www.fei.com/products/tem/tecnai-g2-spirit-for-life-sciences/#gsc.tab=0
X-ray Diffractometer	Bruker D8 advance	https://www.bruker.com/en/products-and-solutions/diffractometers-and-scattering-systems/x-ray-diffractometers/d8-advance-family/d8-advance.html
UV-Visible spectrophotometer	Jasco V-670	https://www.jasco.de/en/content/V-670/~nm.13~nc.407/V-670-UV-VIS-NIR-Spectrophotometer.html
X-ray photoelectron microscope	Thermo Scientific	https://www.thermofisher.com/in/en/home/electron-microscopy/products/xps-instruments/k-alpha.html
Micro-Raman spectrometer	Horiba LabRam	https://www.horiba.com/ind/scientific/products/detail/action/show/Product/labram-hr-evolution-1083/

RESOURCE AVAILABILITY

Lead contact

Further information and requests for resources and reagents should be directed to and will be fulfilled by the lead contact, Prof. S. Venugopal Rao (soma_venu@uohyd.ac.in).

Materials availability

This work has not released any new products. This study did not generate new unique reagents.

Date and code availability

The data reported in the present manuscript can be shared by the corresponding author upon reasonable request.

The codes used in this work can be shared upon reasonable requests.

METHOD DETAILS

Silver nano-dendrite formation

Silver nano-dendrites were synthesized by adopting a low-cost, simple method of electroless-etching. Firstly, a 3" Si wafer was cleaned with acetone and diluted HF to remove chemical residues and native oxides. The cleaned Si wafer was immersed in (30 mM) $AgNO_3$ and (4.6 M) HF composed electrolytic solution for dendrite formation at 30°C. Subsequently, the dendrite samples were cleaned with DI water and dried in an ambient atmosphere. The cleaned 3" AgNDs sample (substrate) was fragmented to a 1 cm^2 models for subsequent studies.

Gold nanoparticle decoration

The stability, compatibility, sensibility, and commercialization of the as-prepared AgNDs substrates are greatly enriched by incorporating AuNPs under the facile galvanic deposition approach. In this process, AgNDs samples were immersed in 1 mM HAuCl4::5 mM HF solution at 30 min, 1 hour, 2 hours, and 3 hours immersion time to get a various density distribution of AuNPs over the AgNDs surface.

Characterization techniques

Morphological examination using a field emission scanning electron microscope (FESEM; Carl ZEISS, Ultra 55–5 eV for imaging, and 20 eV for EDX). The corresponding elemental mapping was performed on AgNDs using the Energy-dispersive X-ray spectroscopy (EDS) technique. X-ray photoelectron spectroscopy (XPS) analysis was accomplished using a Thermo Scientific (K-Alpha-KAN9954133) instrumental setup to confirm the metallic nature of the formed structure. Transmission electron microscope (TEM; Technai, equipped with a thermo-ionic electron gun working at 200 keV) and X-ray diffraction (XRD-Bruker D8 advance) investigations were used to confirm the crystalline quality of the AgNDs and AgNDs@AuNPs. The optical reflection was evaluated by a UV-Visible spectrophotometer (UV–Vis–Jasco V-670) to identify the surface plasmon resonance band for different SERS activities. Eventually, visualization of the near-field enhancement around the NDs was explored by simulations with the support of COMSOL.

Simulation methods

COMSOL Multiphysics was used for simulating the dendrite structures. We have used RF module with frequency domain physics for solving the Maxwell's equations using Comsol. Electromagnetic wave polarized in the X-direction and propagating in the Y-direction with 532 nm wavelength was used for excitation. Dielectric function for Ag and Au were taken from the Johnson's work (Johnson and Christy, 1972).

Surface enhanced Raman spectroscopy

A micro-Raman spectrophotometer (Horiba LabRam Raman Spectrometer) was employed to study essential aspects of molecular detection under Nd:YAG laser excitation. The SERS activity has been tested with various kinds of probe molecules like (i) dyes (crystal violet - CV) (ii) explosive molecule (ammonium nitrate - AN) (iii) pesticide molecule (thiram) and (iv) biomolecules, especially DNA bases (adenine, cytosine), which could be a DNA and RNA builder and tracing of these solutions is essential in biomarker investigations along with antibiotics (penicillin-G, kanamycin, and ampicillin) that are effective in preventing and treating infections in humans and animals. For achieving a better consistency in the Raman signal, the measurements were performed using a 50X objective, 10 s acquisition time and using 532 nm excitation. The spot size estimated at the focus was ~1.5 μm.

QUANTIFICATION AND STATISTICAL ANALYSIS

The limit of detection (LOD) was extracted by exploring the Raman peaks of CV, adenine, cytosine, penicillin-G, kanamycin, ampicillin, AN, and thiram located at 918 cm^{-1}, 722 cm^{-1}, 792 cm^{-1}, 985 cm^{-1}, 975 cm^{-1}, 988 cm^{-1}, 1045 cm^{-1}, 1384 cm^{-1}, respectively. Figures S1A, S2A, S2C, S3A, S3C, S4E, S4A, and S5A present the intensity versus analyte concentration plot, the corresponding linear fits at lower concentrations are also shown in Figures S1–S5. The LOD is expressed as $3\sigma/b$, where σ is the SD of non-SERS substrate (i.e. Silicon), and *b* is the slope of linear fit [Figures S1B, S2B, S2D, S3B, S3D, S3F, S4B, S5B]. The LODs extracted were found to be 348 p.m., 2, 28, 2, 56, 4, 5, and 2 nM, for CV, adenine, cytosine, penicillin-G, kanamycin, ampicillin, AN, and thiram, respectively.